Summer 7-2017

Progress Towards Competitive III-V Infrared Detectors: Fundamental Material Characterization and Techniques

Emil A. Kadlec
University of New Mexico

Progress Towards Competitive III-V Infrared Detectors: Fundamental Material Characterization and Techniques

by

Emil A. Kadlec

B.S., Electrical Engineering, University of New Mexico, 2009
M.S., Electrical Engineering, University of New Mexico, 2011

DISSERTATION

Submitted in Partial Fulfillment of the
Requirements for the Degree of

Doctor of Philosophy
Engineering

The University of New Mexico

Albuquerque, New Mexico

July, 2017

Dedication

To my wife, Mallory, my son, Carver, and the one on the way, thank you for all of the support and love you have given me.

Acknowledgments

I would like to acknowledge and thank my parents, Emil and Diana, who have shown me an immense amount of support through the entirety of my life. I am beyond grateful to have parents such as you.

Secondly, I would like to thank Dr. Eric Shaner. Your mentorship has been an invaluable asset through the duration of this research. I thank you for the helpful discussions, straightforward guidance, and impressive show of free-hand optical alignment. These experiences will never be taken for granted.

To my colleagues at Sandia National Laboratories[1], thank you all for the help, patience, and teachings through the years. It has been a one-of-a-kind experience to be able to work with you all.

Lastly, I would like to thank my wife, Mallory, for venturing through the process of obtaining this degree with me. It is hard to put into words what the support and encouragement you have given me have done for me along this journey.

[1]Sandia National Laboratories is a multimission laboratory managed and operated by National Technology and Engineering Solutions of Sandia, LLC., a wholly owned subsidiary of Honeywell International, Inc., for the U.S. Department of Energys National Nuclear Security Administration under contract DE-NA0003525.

Progress Towards Competitive III-V Infrared Detectors: Fundamental Material Characterization and Techniques

by

Emil A. Kadlec

B.S., Electrical Engineering, University of New Mexico, 2009
M.S., Electrical Engineering, University of New Mexico, 2011

Ph.D., Engineering, University of New Mexico, 2017

Abstract

Measurement of recombination mechanisms provides critical feedback on the material quality of semiconductors. Strained layer type-II superlattices (T2SLs) have seen a recent increase in interest as they possess intriguing properties making them prime candidates for use as infrared detectors. As T2SL-based detectors approach the performance of industry-standard $Hg_{1-x}Cd_xTe$ photodetectors, measurement of the carrier lifetime is becoming increasingly important. A comparison of the lifetime measurement techniques time-resolved photoluminescence, frequency-modulated photoluminescence, time-resolved microwave reflectance, and frequency-modulated conductance is made. Although photoluminescence-based measurement techniques are more common in literature, it is shown that the microwave reflectance-based measurement technique is able to probe lower carrier densities and, therefore, more accurately measure minority carrier lifetime in low-doped samples.

In addition to the lifetime measurement comparison, using a multiple harmonic

approach based on the frequency-modulated photoconductivity method, the recombination mechanisms are measured in an InAs/$InAs_{1-x}Sb_x$ T2SL at a temperature of 100 K. The second harmonic of the generated carrier density is dependent on the high-injection recombination mechanisms and not the minority carrier recombination, enabling accurate extraction of parameters governing high-injection recombination. From these measurements, it is found that the Shockley-Read-Hall lifetime is 3.47 μs $\pm$100 ns, the radiative recombination is 1×10^{-10} cm^3s^{-1}, and the Auger recombination coefficient is 2.29×10^{-26} cm^6s^{-1}, agreeing well with the more-readily used time-resolved microwave reflectance measurement. With this approach, characterization can be performed using basic laboratory equipment without the need of high-end laser systems or fast electronics.

The minority carrier lifetime (τ_{MC}) and equilibrium electron concentration (i.e. the doping level, n_0) are both important values that directly determine diffusion current in infrared photodetectors utilizing n-type absorbing regions. Here, time-resolved microwave reflectance measurements are used to non-destructively measure both of these values in mid-wave infrared InAs/$InAs_{1-x}Sb_x$ type-II superlattices with varying n-type doping levels between 2×10^{14} cm^{-3} and 2×10^{16} cm^{-3}. The measured data are analyzed using carrier recombination theory to determine the doping level ranges where Shockley-Read-Hall (SRH), radiative, and Auger recombination limit τ_{MC}. The optimal doping level, which minimizes dark current, is experimentally determined and corresponds to the electron density at which τ_{MC} switches from SRH limited to Auger limited behavior. A comparison of two InAs/$InAs_{1-x}Sb_x$ photodetectors of different equilibrium electron densities demonstrates a decrease in dark current for a doping level near the optimal $n_0\tau_{MC}$ product.

Contents

List of Figures

List of Figures

Chapter 1

Introduction

1.1 Infrared Radiation

In the early 1800's Sir Frederick William Herschel made his improbable discovery of infrared radiation. While measuring the temperature of different spectral regions of sunlight refracted from a prism, Herschel, using the edges of the visible spectrum as the control, discovered the highest temperature was recorded just past the visible red light. The discovery of what Herschel described as calorific rays, now commonly known as infrared radiation, was the first instance of recorded proof of light beyond the visible spectrum. Flash forward two centuries and the infrared spectrum has found a home in many different technological applications such as telecommunications, spectroscopy, and thermal imaging to name a few.

1.2 Infrared Spectrum

The spectral absorption of Earth's atmosphere plays a significant role in the propagation of infrared radiation as it severely limits the transmission of particular wavelengths. These limitations, mostly due to molecular and chemical absorption, reduce the useful distance light may travel. For example, Fig. 1.1 shows the atmospheric transmission of $2-16\mu m$ light for a 15 cm path length in Albuquerque, New Mexico, a relatively dry climate at an elevation of roughly 5,300 feet. It can be seen that specific regions of high transmission exist, known as atmospheric windows. These windows determine specific spectral infrared regions known as the near-infrared (NIR) consisting of 0.75-1.4 μm, short-wavelength infrared (SWIR) consisting of 1.4-3 μm, mid-wavelength infrared (MWIR) consisting of 3-8 μm, long-wavelength infrared (LWIR) consisting of 8-15 μm, and the far-infrared (FIR) consisting of 15-1000 μm. The NIR region has a broad spectrum of uses that includes NIR spectroscopy, currently one of the fastest growing analytical methods in pharmaceutical technology [1]. The SWIR region is most known for its use in telecommunications, namely the particular wavelength $\lambda = 1.55\mu m$. The MWIR region is where blackbody radiation peaks for hot objects (e.g. rockets) making this a very appealing region for detection. The LWIR region is where peak blackbody emission resides for objects near room temperature, such as humans, making this another appealing region for detection. The FIR region is another region with largely varying applications, one such application is for rotational-mode molecular spectroscopy [2]. The major focus in this dissertation will be on the characterization of material designed for use as a medium for high-performance detection in the MWIR and LWIR regions. These spectral regions present technological challenges with potential for further development, which

will be discussed further in the following sections.

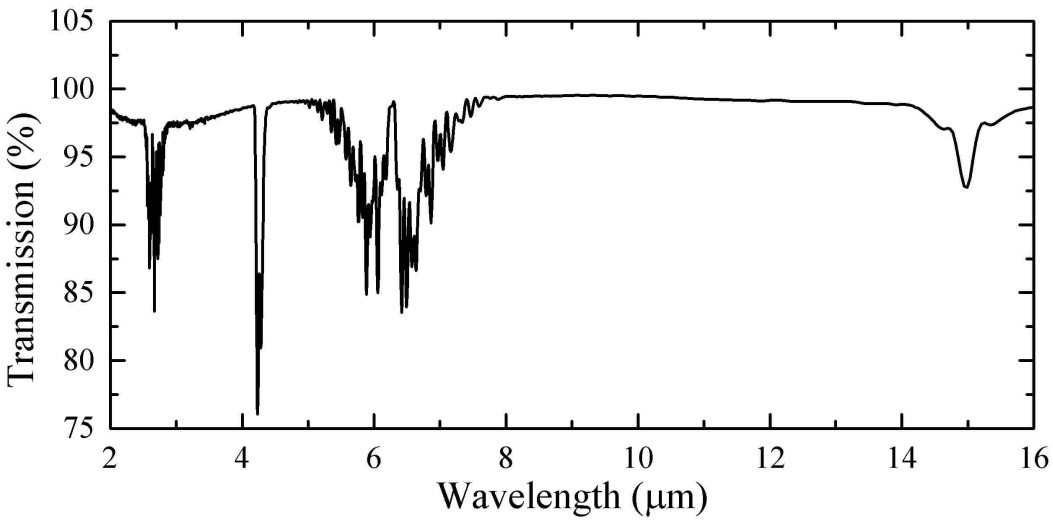

Figure 1.1: Atmospheric transmission in the infrared region ($\lambda = 2 - 16\mu m$) for a 15 cm path length in Albuquerque, New Mexico, a relatively dry climate at an elevation of roughly 5,300 feet. The MWIR and LWIR regions are shown.

1.3 Infrared Photodetection

Infrared photodection has seen vast development in the past century resulting in its use in many different sensing and imaging applications. Of these applications, achieving minimal dark current is especially challenging in photodetectors designed for the MWIR and LWIR regions due to obstacles arising from material quality and small-bandgap energies. There are many different types of materials used for detection in these regions, such as, to name a few, InSb, HgCdTe, and PbSe. The industry standard for detection in these regions is HgCdTe, mainly due to its compositional spectral coverage (E_g = 1-24 μm) and crystalline quality which helps contribute to lower dark currents [3]. The dominance HgCdTe holds in the infrared detection field

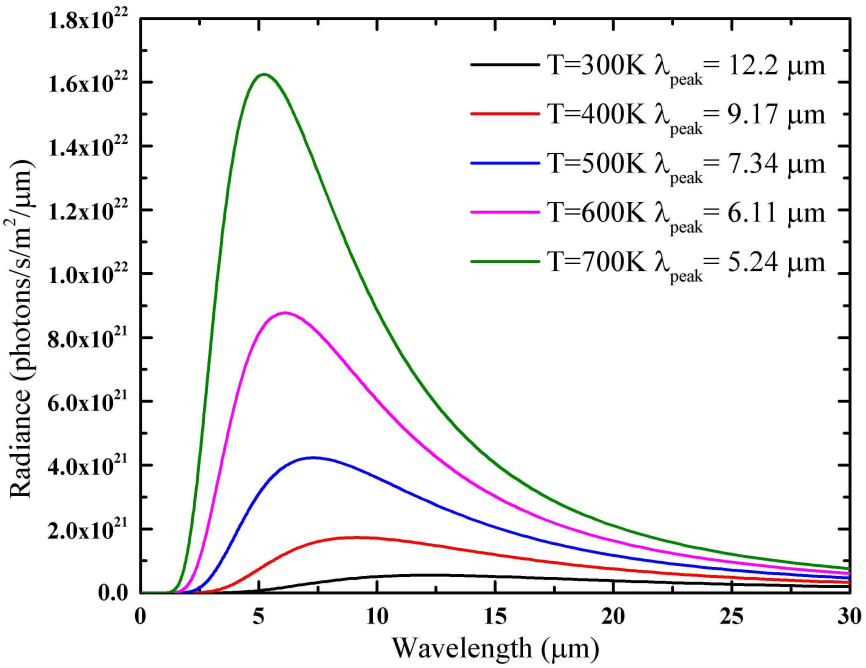

Figure 1.2: Blackbody radiance for various temperatures. Peak emission for a 300 K and 700 K object is 12.23 μm and 5.24 μm, respectively.

didn't happen overnight, in fact, it has taken nearly 60 years of research and production for HgCdTe detectors to be where they are today. This prolonged effort in development has taken LWIR HgCdTe detectors to the point where minority carrier lifetime is intrinsically limited [4], meaning further development in HgCdTe based detectors for the LWIR region may be limited. To continue development of infrared sensing, new material systems must be considered, such as strained-layer type-II superlattices (T2SL).

1.4 Strained Layer Type-II Superlattices

The first published proposal for a semiconductor superlattice (SL) was by Esaki and Tsu in the early 1970's [5]. This proposal was based around changes in doping or composition which would create a one-dimensional periodic potential (i.e. superlattice). As the periodicity of the potential is brought to small thicknesses, the wave function of the two materials will begin to interact. The overlap of the wavefunction will allow and inhibit specific bands, thus, inducing mini-bands of allowable energy levels, shown in Fig. 1.3, which are dependent on the composition of the superlattice. The resultant bandstructure of the superlattice allows for many unique physical parameters such as a bandgap energy that is smaller than the constituent materials which can be engineered to a specific wavelength of interest. Such constraints of growth (i.e. abrupt compositional change), lend the growth of T2SLs to the III-V material system very well due to the excellent control of composition and closely lattice matched material systems, namely the 6.1 $\mathring{A}$ family (InAs, GaSb, InAsSb, and AlSb). An added benefit is the availability of closely lattice matched wafers, such as GaSb.

The unique material characteristics possessed by T2SLs have sparked much interest in not only the detector community, but the laser [6] and LED [7], [8] fields. In 1977, Sai-Halasz and Esaki proposed the first T2SL, based on InAs/GaSb [9], which was shown experimentally a year later [10]. In 1987, Smith and Mailhoit proposed using the InAs/GaSb T2SL as an infrared detector [11]. Due to the interaction of electrons and holes as a result of tunneling through barriers, T2SLs offer larger electron and hole effective masses compared to conventional bulk material such as

HgCdTe. The larger effective masses will likely reduce tunneling currents in T2SL detector designs, which is a major contributor to dark current in HgCdTe. Due to the inherent strain and inhibited bands, it was predicted that the Auger lifetime of T2SL would be competitive with HgCdTe [12]. Later on, it was shown experimentally by Youngdale *et al.* that the InAs/Ga(In)Sb T2SL displayed an Auger lifetime of over two orders of magnitude greater than HgCdTe [13]. These promising results and theory have led to the further development of T2SLs for detector applications as they show the possibility of III-V superlattice-based detectors outperforming HgCdTe detectors.

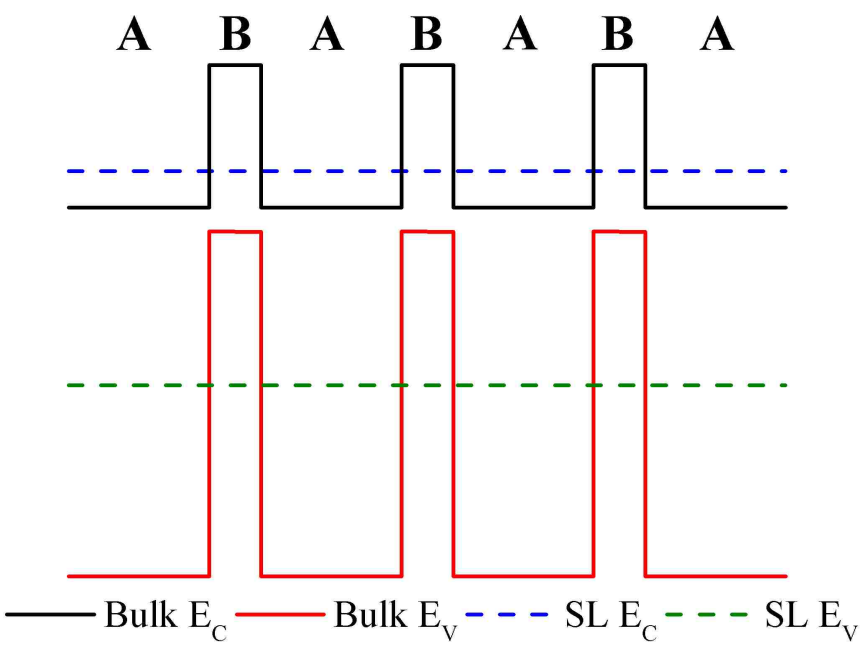

Figure 1.3: Band diagram of several periods of a generic T2SL. The solid curves represent bulk conduction and valence bands. The dashed curves represent the superlattice conduction and valence band found from the edges of the mini-bands.

1.4.1 InAs/GaSb Superlattice

Over the past two decades, the InAs/GaSb material system has seen the most attention for application in T2SL-based detectors as they have been theorized to surpass the dark-current performance of HgCdTe detectors [12]–[14]. The extensive effort in development of this material system has seen the application of InAs/GaSb SLs in focal plane arrays in the MWIR [15], [16] and the LWIR [17] regions, with single detectors being background limited up to 180 K [18]. Although the performance of these devices is approaching the performance of HgCdTe devices [4], this material system has been limited by parasitic Shockley-Read-Hall (SRH) defects resulting in short minority carrier lifetimes. For example, studies of InAs/GaSb T2SL in the MWIR have shown minority carrier lifetimes in the range of 80-100 ns [19]–[22] and in the LWIR 10-30 ns [20], [23]–[25]. A study investigating carrier lifetimes of InAs/GaSb T2SL with varying GaSb thickness as well as bulk growth of InAs and GaSb has suggested a native defect associated with GaSb could be the cause of the relatively short minority carrier lifetimes [21]. Due to the limitations set by the intrinsic SRH lifetime on InAs/GaSb, new material systems are seeing more interest for T2SL incorporation in detectors designs, such as InAs/InAsSb.

1.4.2 InAs/InAsSb Superlattice

As an alternative to the InAs/GaSb system, InAs/InAsSb T2SLs have been proposed as a Ga-free material system with hopes of longer minority carrier lifetimes. This T2SL still retains similar characteristics to the InAs/GaSb SL, such as bandgap tuning throughout the MWIR and LWIR regions [26] and reduction in Auger re-

combination as compared to HgCdTe. Studies on the minority carrier lifetime of InAs/InAsSb T2SLs in the MWIR region have shown minority carrier lifetimes on the order of $2.3 \times 10 \mu s$ [22] and in the LWIR region minority carrier lifetimes of 412 ns [27]. High-injection studies of carrier recombination have shown Auger recombination in LWIR InAs/InAsSb to be on the order of $10^{-25} cm^6/s$, roughly an order of magnitude less than HgCdTe [28]. As a result of these studies showing improved minority carrier lifetime and comparable Auger recombination to InAs/GaSb, the detector community has shown excitement in the InAs/InAsSb T2SL leading to recent investigations in vertical transport properties [29], [30] and basic radiation studies [31], again showing promise for the InAs/InAsSb T2SL as an infrared detector.

1.5 Type-II superlattice detector design

Three main mechanisms contribute to dark current in infrared photodiodes, thus limiting device performance. The dark current of a photodiode can be described as [32]

$$I_{dark} = I_{GR} + I_{diff} + I_{surf}, \tag{1.1}$$

where I_{GR} is the current associated with carriers generated from SRH traps in the depletion region, I_{diff} is the current associated with carriers being thermally generated, and I_{surf} is the current associated with surface states. Not only does working in the III-V's offer better material quality, but it also opens up the door for the incorporation of different materials into detector design. The inclusion of these differing materials allows for creative device structures that better mitigate dark current mechanisms. Basic T2SL photodiode designs have been shown, however due to SRH

generation in the depletion regions the dark current in these devices is rather high [33], [34]. Designs to suppress these dark current mechanisms have been shown and include the M-structure [35], [36], the W-structure [37], [38], and the nBn structure [32]. Of these designs the nBn structure, shown in Fig. 1.4, has recently seen the most attention due to the simplicity of its design and dark current performance, which theoretically eliminates surface current and greatly reduces SRH generation currents [39]. The nBn detector design consists of a n-type contact, a barrier region, and an n-type absorber. For the nBn structure the generation-recombination current and diffusion current, with the assumption that the diffusion length is longer than the absorber thickness, are described as [4], [32]

$$J_{GR} = \frac{n_i W_{dep}}{\tau_{SRH}}, \tag{1.2}$$

$$J_{diff} = \frac{n_i^2 W_{abs}}{n_0 \tau_{MC}}, \tag{1.3}$$

where n_i is the intrinsic carrier density, q is the electron charge, W_{dep} is the depletion width, τ_{SRH} is the SRH lifetime of minority carriers, W_{abs} is the thickness of the absorber, n_0 is the electron doping, and τ_{MC} is the minority carrier lifetime. Due to the reduction of the depletion region, J_{GR} has been greatly reduced leaving diffusion current as the dominant dark current mechanism. It should be noted from Eq. 1.3, that the diffusion current is inversely proportional to the product of the electron doping density and minority carrier lifetime of the absorber region. This characteristic will be investigated in a later chapter of this dissertation showing the relation of lifetime measurements to predicted dark-diffusion current.

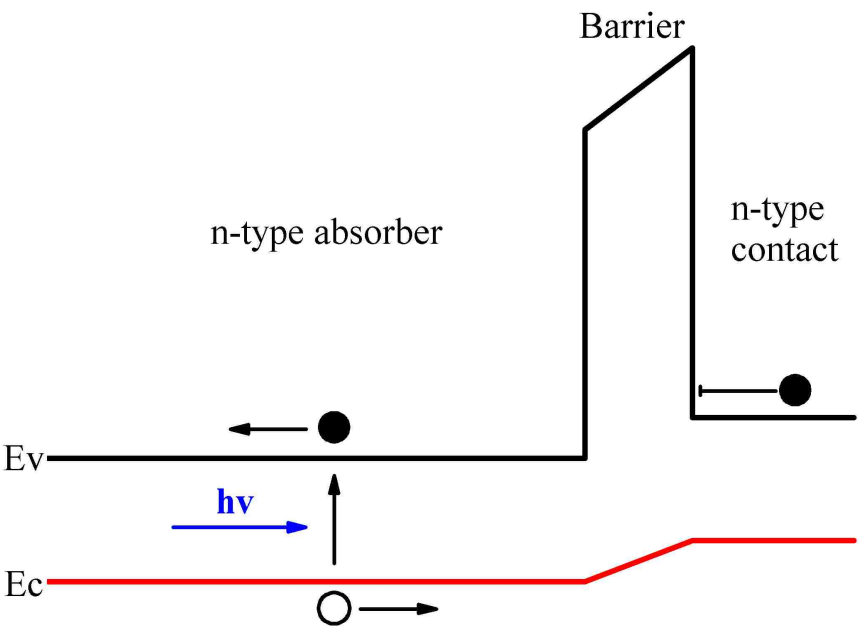

Figure 1.4: Band diagram of ideal *nBn* detector structure under biased operating conditions. The design consists of an *n*-type absorber, barrier region, and *n*-type contact. The barrier region blocks majority carrier flow making this a minority carrier device. Excited electron-hole pairs in the absorber region are allowed to flow through device.

1.6 Organization of Dissertation

The main focus of this dissertation is to show proper carrier lifetime measurement techniques and how to implement these measurements into material quality predictions. Chapter two will give a background of semiconductor physics with a focus on non-equilibrium charge carrier dynamics. Chapter 3 will give a background of carrier lifetime measurement techniques with an emphasis on an extension of the frequency modulated photoconductivity method. This extension, which looks at the generation of a second harmonic, will prove worthy of consideration for future lifetime measurement approaches. Chapter 4 shows a study of 14 different InAs/InAsSb

T2SL samples of varying doping density. This study will show correlation between measurement theory and device dark current data.

1.7 References

[1] M. Jamrgiewicz, "Application of the near-infrared spectroscopy in the pharmaceutical technology," *Journal of Pharmaceutical and Biomedical Analysis*, vol. 66, pp. 1 –10, 2012, ISSN: 0731-7085. DOI: https://doi.org/10.1016/j.jpba.2012.03.009. [Online]. Available: http://www.sciencedirect.com/science/article/pii/S073170851200132X.

[2] R. H. Hunt, R. A. Leacock, C. W. Peters, and K. T. Hecht, "Internal-rotation in hydrogen peroxide: The far-infrared spectrum and the determination of the hindering potential," *The Journal of Chemical Physics*, vol. 42, no. 6, pp. 1931–1946, 1965. DOI: 10.1063/1.1696228. eprint: http://dx.doi.org/10.1063/1.1696228. [Online]. Available: http://dx.doi.org/10.1063/1.1696228.

[3] M. A. Kinch, "Fundamental physics of infrared detector materials," *J. Electron. Mat.*, vol. 29, pp. 809–817, 2000.

[4] D. R. Rhiger, "Performance comparison of long-wavelength infrared type-ii superlattice devices with HgCdTe," *J. Electron. Mat.*, vol. 40, pp. 1815–1822, 2011.

[5] L. Esaki and R. Tsu, "Superlattice and negative differential conductivity in semiconductors," *IBM J. Res. Develop.*, vol. 14, p. 61, 1970.

[6] E. F. Schubert, A. Fischer, Y. Horikoshi, and K. Ploog, "Gaas sawtooth superlattice laser emitting at wavelengths $\lambda > 0.9\mu m$," *Applied Physics Letters*, vol. 47, no. 3, pp. 219–221, 1985. DOI: 10.1063/1.96223. eprint: http://dx.doi.org/10.1063/1.96223. [Online]. Available: http://dx.doi.org/10.1063/1.96223.

[7] E. J. Koerperick, J. T. Olesberg, T. F. Boggess, J. L. Hicks, L. S. Wassink, L. M. Murray, and J. P. Prineas, "InAs/GaSb cascaded active region superlattice light emitting diodes for operation at 3.8 μm," *Appl. Phys. Lett.*, vol. 92, p. 121 106, 2008.

[8] E. J. Koerperick, D. T. Norton, J. T. Olesberg, B. V. Olson, J. P. Prineas, and T. F. Boggess, "Cascaded superlattice InAs/GaSb light-emitting diodes for operation in the long-wave infrared," *IEEE J. Quant. Electron.*, vol. 47, pp. 50–54, 2011.

[9] G. A. Sai-Halasz, R. Tsu, and L. Esaki, "A new semiconductor superlattice," *Appl. Phys. Lett.*, vol. 30, pp. 651–653, 1977.

[10] H. Sakaki, L. Chang, G. Sai-Halasz, C. Chang, and L. Esaki, "Two-dimensional electronic structure in inas-gasb superlattices," *Solid State Communications*, vol. 26, no. 9, pp. 589 –592, 1978, ISSN: 0038-1098. DOI: http://dx.doi.org/10.1016/0038-1098(78)90770-6. [Online]. Available: http://www.sciencedirect.com/science/article/pii/0038109878907706.

[11] D. L. Smith and C. Mailhiot, "Proposal for strained type II superlattice infrared detectors," *J. Appl. Phys.*, vol. 62, pp. 2545–2548, 1987.

[12] C. H. Grein, P. M. Young, and H. Ehrenreich, "Minority carrier lifetimes in ideal InGaSb/InAs superlattices," *Appl. Phys. Lett.*, vol. 61, pp. 2905–2907, 1992.

[13] E. R. Youngdale, J. R. Meyer, C. A. Hoffman, F. J. Bartoli, C. H. Grein, P. M. Young, H. Ehrenreich, R. H. Miles, and D. H. Chow, "Auger lifetime enhancement in InAs-$Ga_{1-x}In_xSb$ superlattices," *Appl. Phys. Lett.*, vol. 64, pp. 3160–3162, 1994.

[14] C. H. Grein, H. Cruz, M. E. Flatté, and H. Ehrenreich, "Theoretical performance of very long wavelength InAs/InGaSb superlattice based infrared detectors," *Appl. Phys. Lett.*, vol. 65, pp. 2530–5232, 1994.

[15] R. Rehm, M. Walther, J. Schmitz, J. Fleibner, F. Fuchs, J. Ziegler, and W. Cabanski, "InAs/GaSb superlattice focal plane arrays for high-resolution thermal imaging," *Opt. Electron. Rev.*, vol. 14, pp. 19–24, 2006.

[16] H. S. Kim, E. Plis, J. B. Rodriguez, G. D. Bishop, Y. D. Sharma, L. R. Dawson, S. Krishna, J. Bundas, R. Cook, D. Burrows, R. Dennis, K. Patnaude, A. Reisinger, and M. Sundaram, "Mid-IR focal plane array based on type-II InAs/GaSb strain layer superlattice detector with nBn design," *Appl. Phys. Lett.*, vol. 92, p. 183 502, 2008.

[17] A. Haddadi, S. Ramezani-Darvish, G. Chen, A. M. Hoang, B.-M. Nguyen, and M. Razeghi, "High operability 1024x1024 long wavelength type-II superlattice focal plane array," *IEEE J. Quant. Electron.*, vol. 48, pp. 221–228, 2012.

[18] M. Razeghi, S. A. Pour, E. K. Huang, G. Chen, A. Haddadi, and B. M. Nguyen, "Type-ii InAs/GaSb photodiodes and focal plane arrays aimed at high operating temperatures," *Opt. Electron. Rev.*, vol. 19, pp. 261–269, 2011.

[19] D. Donetsky, S. P. Svensson, L. E. Vorobjev, and G. Belenky, "Carrier lifetime measurements in short-period InAs/GaSb strained-layer superlattice structures," *Appl. Phys. Lett.*, vol. 95, p. 212 104, 2009.

[20] D. Donetsky, G. Belenky, S. Svensson, and S. Suchalkin, "Minority carrier lifetime in type-2 InAs-GaSb strained-layer superlattices and bulk HgCdTe materials," *Appl. Phys. Lett.*, vol. 97, p. 052 108, 2010.

[21] S. P. Svensson, D. Donetsky, D. Wang, H. Hier, F. J. Crowne, and G. Belenky, "Growth of type II strained layer superlattice, bulk InAs and GaSb materials for minority lifetime characterization," *J. Crystal Growth*, vol. 334, pp. 103–107, 2011.

[22] B. V. Olson, E. A. Shaner, J. K. Kim, J. F. Klem, S. D. Hawkins, L. M. Murray, J. P. Prineas, M. E. Flatté, and T. F. Boggess, "Time-resolved optical measurements of minority carrier recombination in a mid-wave infrared InAsSb alloy and InAs/InAsSb superlattice," *Appl. Phys. Lett.*, vol. 101, p. 092 109, 2012.

[23] B. C. Connelly, G. D. Metcalfe, H. Shen, and M. Wraback, "Direct minority carrier lifetime measurements and recombination mechanisms in long-wave infrared type II superlattices using time-resolved photoluminescence," *Appl. Phys. Lett.*, vol. 97, p. 251 117, 2010.

[24] S. Bandara, P Maloney, N. Baril, J. Pellegrino, and M. Tidrow, "Doping dependence of minority carrier lifetime in long-wave Sb-based type II superlattice infrared detector materials," *Proc. of SPIE*, vol. 50, p. 061 015, 2011.

[25] H. J. Haugan, G. J. Brown, S. Elhamri, S. Pacley, B. V. Olson, and T. F. Boggess, "Post growth annealing study on long wavelength infrared InAs/GaSb superlattices," *J. Appl. Phys.*, vol. 111, p. 053 113, 2012.

[26] D. Lackner, M. Steger, M. L. W. Thewalt, O. J. Pitts, Y. T. Cherng, S. P. Watkins, E. Plis, and S. Krishna, "InAs/InAsSb strain balanced superlattices for optical detectors: Material properties and energy band simulations," *J. Appl. Phys.*, vol. 111, p. 034 507, 2012.

[27] E. H. Steenbergen, O. O. Cellek, D. Lubyshev, Y. Qiu, J. M. Fastenau, A. W. K. Liu, and Y.-H. Zhang, "Study of the valence band offsets between inas and inassb alloys," *Proc. of SPIE*, vol. 8268, 82680K–1, 2012.

[28] B. V. Olson, C. H. Grein, J. K. Kim, E. A. Kadlec, J. F. Klem, S. D. Hawkins, and E. A. Shaner, "Auger recombination in long-wave infrared inas/inassb type-ii superlattices," *Appl. Phys. Lett.*, vol. 107, no. 26, 261104, 2015. DOI: `http://dx.doi.org/10.1063/1.4939147`. [Online]. Available: `http://scitation.aip.org/content/aip/journal/apl/107/26/10.1063/1.4939147`.

[29] B. V. Olson, L. M. Murray, J. P. Prineas, M. E. Flatté, J. T. Olesberg, and T. F. Boggess, "All-optical measurement of vertical charge carrier transport in mid-wave infrared InAs/GaSb type-II superlattices," *Appl. Phys. Lett.*, vol. 102, p. 202 101, 2013.

[30] B. V. Olson, J. F. Klem, E. A. Kadlec, J. K. Kim, M. D. Goldflam, S. D. Hawkins, A. Tauke-Pedretti, W. T. Coon, T. R. Fortune, E. A. Shaner, and M. E. Flatté, "Vertical hole transport and carrier localization in InAs/inas$1-x$sb$x$ type-ii superlattice heterojunction bipo-

lar transistors," *Phys. Rev. Applied*, vol. 7, p. 024 016, 2 2017. DOI: 10.1103/PhysRevApplied.7.024016. [Online]. Available: http://link.aps.org/doi/10.1103/PhysRevApplied.7.024016.

[31] L. Höglund, D. Z. Ting, A. Khoshakhlagh, A. Soibel, A. Fisher, C. J. Hill, S. Keo, S. Rafol, and S. D. Gunapala, "Influence of proton radiation on the minority carrier lifetime in midwave infrared inas/inassb superlattices," *Applied Physics Letters*, vol. 108, no. 26, 263504, 2016. DOI: http://dx.doi.org/10.1063/1.4954901. [Online]. Available: http://scitation.aip.org/content/aip/journal/apl/108/26/10.1063/1.4954901.

[32] S. Maimon and G. W. Wicks, "Nbn detector, an infrared detector with reduced dark current and higher operating temperature," *Appl. Phys. Lett.*, vol. 89, p. 151 109, 2006.

[33] I. Vurgaftman, E. H. Aifer, C. L. Canedy, J. G. Tischler, J. R. Meyer, J. H. Warner, E. M. Jackson, G. Hildebrandt, and G. J. Sullivan, "Graded band gap for dark-current suppression in long-wave infrared W-structured type-II superlattice photodiodes," *Appl. Phys. Lett.*, vol. 89, p. 121 114, 2006.

[34] A. Khoshakhlagh, S. Myers, H. Kim, E. Plis, N. Gautam, S. J. Lee, S. K. Noh, L. R. Dawson, and S. Krishna, "Long-wave InAs/GaSb superlattice detectors based on nBn and pin designs," *IEEE J. Quant. Electron.*, vol. 46, pp. 959–964, 2010.

[35] E. K. Huang, S. A. Pour, M.-A. Hoang, A. Haddadi, M. Razeghi, and M. Z. Tidrow, "Low irradiance background limited type-II superlattice MWIR M-barrier imager," *Optics Lett.*, vol. 37, pp. 2025–2027, 2012.

[36] B.-M. Nguyen, S. Bogdanov, S. A. Pour, and M. Razeghi, "Minority electron unipolar photodetectors based on type II InAs/GaSb/AlSb superlattices for very long wavelength infrared detection," *Appl. Phys. Lett.*, vol. 95, p. 183 502, 2009.

[37] E. H. Aifer, J. G. Tischler, J. H. Warner, I. Vurgaftman, W. W. Bewley, J. R. Meyer, J. C. Kim, L. J. Whitman, C. L. Canedy, and E. M. Jackson, "W-structured type-II superlattice long-wave infrared photodiodes with high quantum efficiency," *Appl. Phys. Lett.*, vol. 89, p. 053 519, 2006.

[38] B. V. Olson, J. K. Kim, E. A. Kadlec, J. F. Klem, S. D. Hawkins, W. T. Coon, T. R. Fortune, A. Tauke-Pedretti, M. A. Cavaliere, and E. A. Shaner, "Optical and electrical properties of narrow-bandgap infrared w-structure superlattices incorporating alas/alsb/alas barrier layers," *Applied Physics Letters*, vol. 108, no. 25, 252104, 2016. DOI: http://dx.doi.org/10.1063/1.4954649. [Online]. Available: http://scitation.aip.org/content/aip/journal/apl/108/25/10.1063/1.4954649.

[39] D. R. Rhiger, E. P. Smith, B. P. Kolasa, J. K. Kim, J. F. Klem, and S. D. Hawkins, "Analysis of iii–v superlattice nbn device characteristics," *Journal of Electronic Materials*, vol. 45, no. 9, pp. 4646–4653, 2016, ISSN: 1543-186X. DOI: 10.1007/s11664-016-4545-y. [Online]. Available: http://dx.doi.org/10.1007/s11664-016-4545-y.

Chapter 2

Background

In the materials world you have conductors, insulators, and semiconductors. A conductor has free electrons allowing current to flow. These types of materials are used for electrical connection between systems, something as simple as household wiring or as complex as integrated circuits. Insulators are materials that do not have free electrons and therefore do not conduct electricity. A common insulator of day-to-day use would be the rubber on a power or USB cord. The semiconductor sits in the middle of the conductor and insulator, as it doesn't necessarily possess the characteristics of either, yet it can be engineered to resemble one or the other under specific circumstances. The ability to be engineered for specific applications will be shown to be a product of the crystal structure of the semiconductor. The most common and well known semiconductor is Silicon due to its importance in the electronics industry. Although Silicon is the backbone of almost every electronic device, it does lack characteristics for some applications, such as an indirect bandgap. Where silicon falls off due to this characteristic, the III-V's (i.e. GaAs) pick up due

to direct bandgaps and other unique characteristics. In this chapter we will take a look at basic semiconductor physics and work towards the complexity of the strained layer type-II superlattice (T2SL) to build a base for the carrier lifetime analysis to come in the following chapters.

2.1 The wave equation

The basic understanding of the discrete energy levels possessed by semiconductors is necessary before devolving into recombination theory. In this section we start from Schrödinger's wave equation to evaluate an electron in a potential barrier and work our way towards semiconductor band structure theory.

In the early 1900's some of the most elegant and renowned theories of physics were born. One of these was the concept of wave-particle duality which states that every object can be described in terms of waves and not only particles. Quantum-scale objects, such as atoms or electrons, are best described by this principle. Many well known physicists, such as Einstein, Bohr, Plank, and de Broglie, put much effort into this concept helping lead Schrödinger to formulate *wave-mechanics* in 1926. The nonrelativistic Schrödinger's wave equation is given by

$$\frac{-\hbar}{2m}\nabla^2\Psi(r,t) + V(r,t)\Psi(r,t) = j\hbar\frac{\partial}{\partial t}\Psi(r,t), \tag{2.1}$$

where $\Psi(r,t)$ is the wave function, $V(r,t)$ is the potential function, and m is the mass of the particle. For an atomic orbital of a hydrogen-like particle the potential

of the electron to proton can be described by Coulomb's law

$$V(r) = \frac{-e^2}{4\pi\epsilon_0 r}, \tag{2.2}$$

where e is the electron charge and ϵ_0 is the permittivity of free space. From separation of variables the time-independent Schrödinger equation for the hydrogen-like particle can be written as

$$\nabla^2\Psi(r,\theta,\phi) + \frac{2m_0}{\hbar}(E - V(r))\Psi(r,\theta,\phi) = 0, \tag{2.3}$$

where m_0 is the mass of the electron. Assuming the time-independent wave function can be written as

$$\Psi(r,\theta,\phi) = R(r)\Theta(\theta)\Phi(\phi), \tag{2.4}$$

using separation-of-variables the solution to Eq. 2.3 can be found through only a few pages of derivations. The solution reveals three quantum numbers, generally described as n, l, and m, which is a result of the electron being bound to a finite region of space. The quantum numbers l and m are found from the θ and ϕ terms. The remaining quantum number, n, is found from the radial term. The energy of the electron may be described as

$$E_n(n) = -\frac{m_0 e^4}{(4\pi\epsilon_0)^2 2\hbar^2 n^2}, \tag{2.5}$$

where n is the principle quantum number as described earlier. From Eq. 2.5, it is seen the energy takes a quantized form dependent on n. It should also be noted that the energy is negative, meaning that the electron is bound to a finite region of space

due to it's interaction with the nucleus of the atom. The wave function of the ground state ($n = 1$, $m = 0$, and $l = 0$) is found to be

$$\Psi_{1,0,0}(r) = \frac{1}{\sqrt{\pi} a_0^{\frac{3}{2}}} e^{\frac{-r}{a_0}}, \tag{2.6}$$

where a_0 is the Bohr radius. The radial probability of the electron state is

$$P_{1,0,0}(r) = \frac{4r^2}{a_0^3} e^{\frac{-2r}{a_0}}. \tag{2.7}$$

Fig. 2.1 shows the radial probability density function of the ground state, it can be seen that the most probable location of the electron is at the Bohr radius. The higher order quantum terms become very interesting to solve and analyze, however these are out of the scope of this dissertation. If the reader is so obliged, Refs. [1] pertains to much finer details from the previous section and are recommended for further reading.

2.2 Band structure theory

Fig. 2.1 shows the radial probability density function of two hydrogen atoms spaced by $6a_0$. It is seen that the probability of the two electrons overlap, meaning that the wavefunctions of the electrons will interact with each other causing a splitting of energy states. This splitting can be explained by the Pauli exclusion principle. Now, imagine that the atom is sitting in a GaAs crystal lattice where the atomic density is on the order of $5 \times 10^{22} cm^{-3}$, obviously there will be a considerable amount of wavefunction overlap in this setting. A general theoretical approach to simulate a

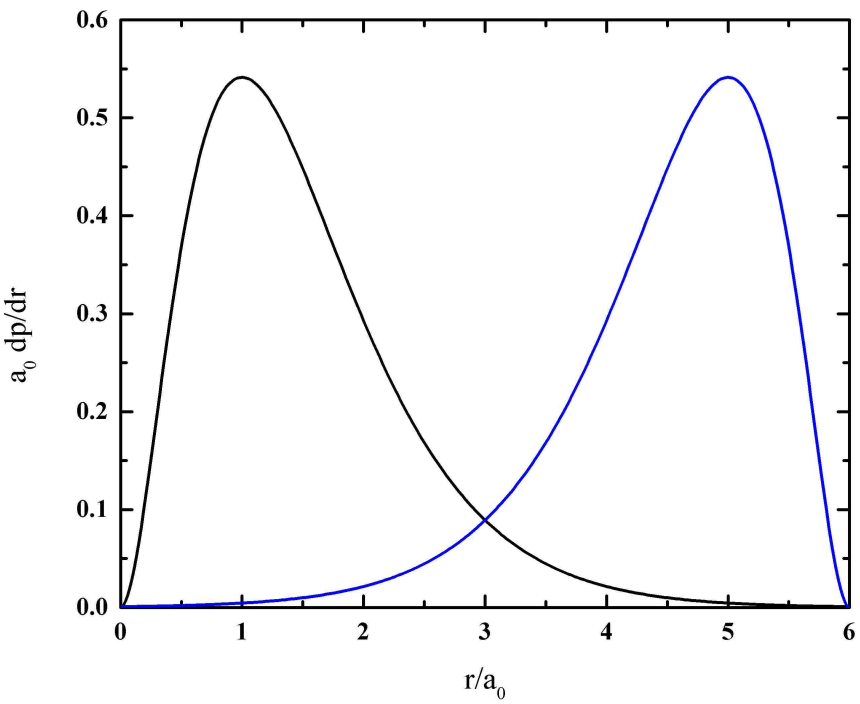

Figure 2.1: The radial probability density function for the ground state of the one electron atom (Hydrogen atom), black curve. The blue curve is the probability density function of another one electron atom at a distance of $6a_0$ from the origin. It can be seen that the probability density functions of the spaced atoms overlap, leading to a splitting of energy states.

period potential is the Kronig-Penny model, which assumes the wave function will take the form of a Bloch function [2]. The resultant form of the wavefunction for a one-dimensional setting is

$$\Psi(x,t) = u(x)e^{j(kx-(E/\hbar)t)}, \tag{2.8}$$

where $u(x)$ is a periodic function and k is the wavevector. For a one-dimensional periodic potential with $E < V_0$ (shown in Fig. 2.2), which applies to an electron bound to the crystal structure, the solutions to E and k are realized when the

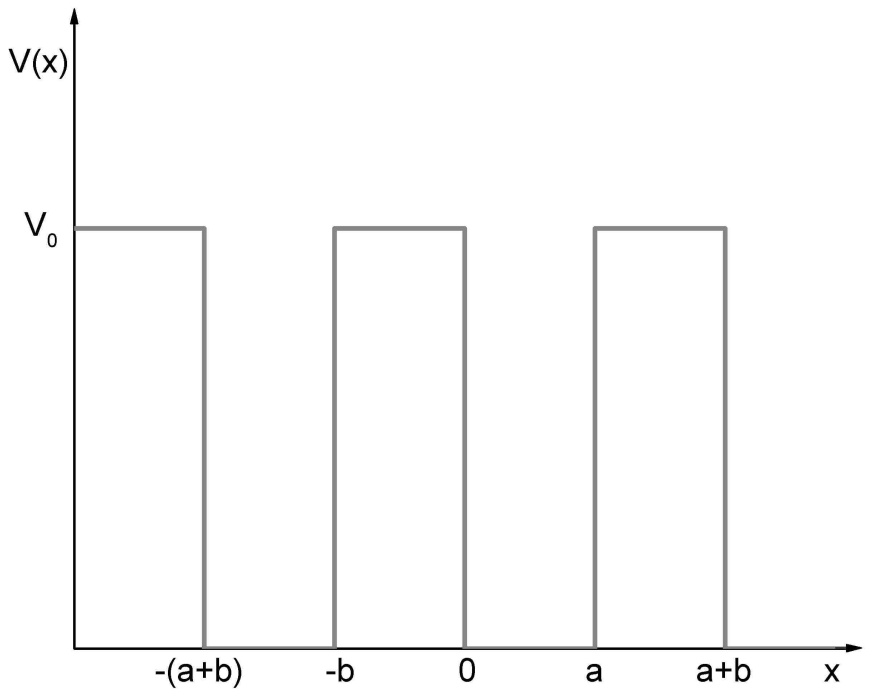

Figure 2.2: The one-dimensional periodic potential function used for the Kronig-Penney model.

following equation is satisfied

$$cos(ka) = F = \frac{\alpha^2 - \beta^2}{2\alpha\beta} sinh(\alpha b) sin(\beta(a-b)) + cosh(\alpha b) cos(\beta(a-b)), \tag{2.9}$$

where

$$\alpha = \frac{\sqrt{2m(V_0 - E)}}{\hbar}, \tag{2.10}$$

and

$$\beta = \frac{\sqrt{2mE}}{\hbar}. \tag{2.11}$$

The solution to Eq. 2.9 becomes interesting when the barrier width approaches zero and the barrier height approaches infinity, yet the product of the two remains finite.

This will simplify Eq. 2.9 to

$$cos(ka) = F = P\frac{sin(\beta a)}{\beta a} + cos(\beta a), \tag{2.12}$$

where

$$P = \frac{mV_0ba}{\hbar^2}. \tag{2.13}$$

It can be seen from Eq. 2.12 that the solution to the righthand side (RHS) of the equation will only exist, or be bound, to the range of ± 1. Solving for energy, E, as a function of k we find the solution in Fig. 2.3, which shows the existence of particular allowed energy bands, as well as disallowed bands. These allowed bands are the basis of the semiconductor energy bands, namely the conduction and valence bands.

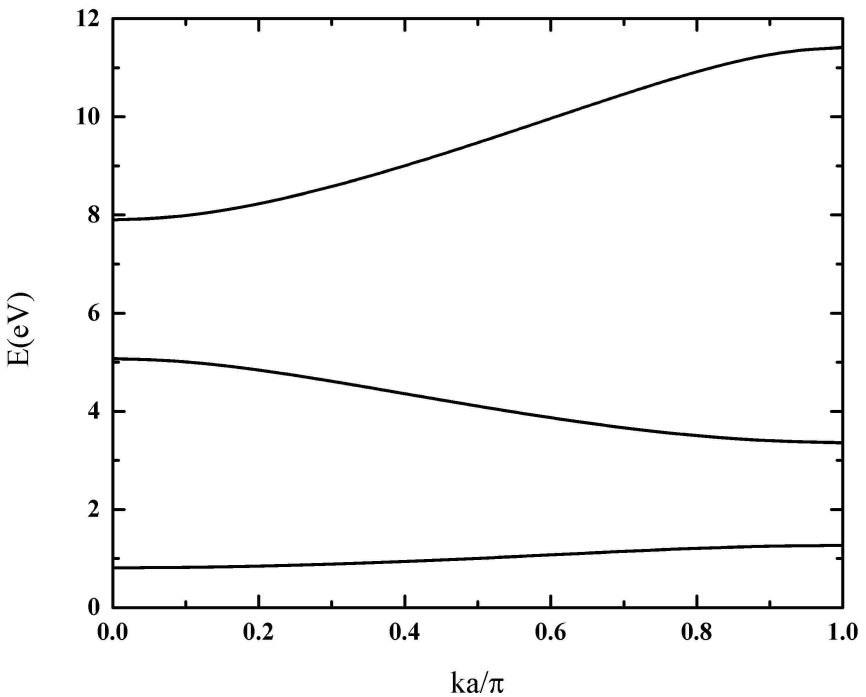

Figure 2.3: E versus k diagram for the reduced-zone representation.

In a semiconductor, an electron may be excited by an external force, such as a rise in temperature or absorption of a photon, and leave the ground state (valence band) to an excited state (conduction band). Because the semiconductor must conserve charge, the process of the electron being excited from the valence band creates an electron hole, or commonly known as a hole. The hole is a state where an electron could exist and maintains a net positive charge. The process of exciting an electron and hole is commonly called creating an electron-hole pair. A generic direct-gap semiconductor band structure as a function of wavevector (k) can be seen in Fig. 2.4. In this example, The conduction band minimum is directly above the valence band maximum. The the valence band is comprised of a heavy hole band, a light hole band, and a split off band. The heavy hole and light hole bands get their names from the effective mass of holes occupying their bands. The effective mass is essentially used to simplify the model of a free particle in a specific band structure. The effective mass is described as

$$\frac{1}{m^*} = \frac{1}{\hbar^2}\frac{d^2E}{dk^2}, \tag{2.14}$$

where m^* is the effective mass of either the hole in the valence bands or an electron in the conduction band. The total effective mass in the valence band takes into account both the heavy and light hole,

$$m_h = (m_{HH}^{\frac{3}{2}} + m_{LH}^{\frac{3}{2}})^{\frac{2}{3}}, \tag{2.15}$$

where m_{HH} is the heavy hole mass and m_{LH} is the light hole mass. The split-off band has an offset from the heavy and light hole bands, because of this offset the split-off band is generally fully occupied. However, the split-off band can interact in Auger processes which will be described in more detail later on in this chapter. The

bandgap energy (E_g), which is the minimal amount of energy it takes to excite an electron out of the valence to the conduction band, is the energy difference of the conduction and valence bands at $k = 0$.

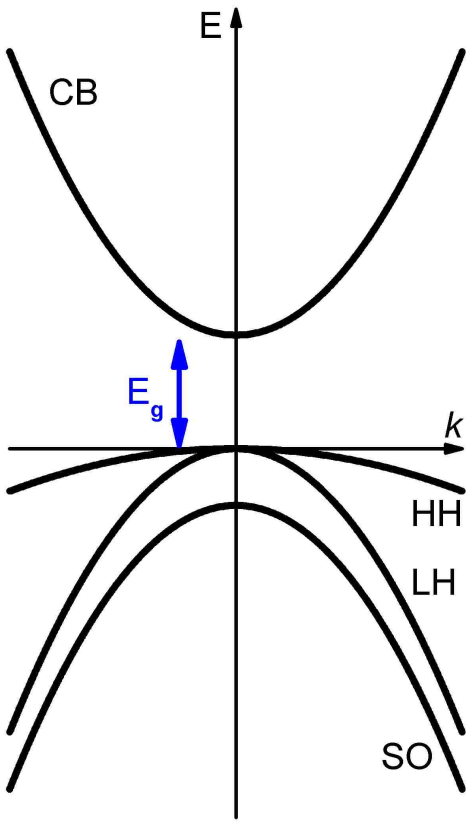

Figure 2.4: Energy band diagram of a generic direct-gap semiconductor. A conduction band, heavy-hole band, light-hole band, and a split-off band are shown. The bandgap energy of the semiconductor is found from the difference of the conduction band minimum and valence band maximum.

2.3 Semiconductor in equilibrium

For a semiconductor in thermal equilibrium at a temperature T, the probability of an electron occupying an electronic state at an energy of E is given by the Fermi-Dirac distribution function

$$f(E) = \frac{1}{e^{\frac{E-E_f}{k_B T}} + 1}, \tag{2.16}$$

where k_B is the Boltzmann constant and E_f is the Fermi energy level (also know as the chemical potential). For a temperature $T = 0$ the probability of an electron filling a state above the Fermi energy is zero. At an infinitely large energy level, the probability of occupation is also zero. These two specific cases make physical sense. For large temperatures, $T \gg 0$, the Fermi-Dirac equation shows a probability of 0.5 for ene. Similarly, the probability of an electron not occupying an electronic state is given by

$$1 - f(E) = \frac{1}{e^{\frac{E_f-E}{k_B T}} + 1}, \tag{2.17}$$

this can also be described as the likelihood of a hole occupying a state in the valence band.

The density of allowed electronic states in the conduction band is written as

$$g_c(E) = \frac{4\pi(2m_e^*)^{3/2}}{h^3}\sqrt{E - E_c}, \tag{2.18}$$

which is valid for $E \geq E_c$. Likewise, the density of allowed states for holes in the valence band is written as

$$g_v(E) = \frac{4\pi(2m_h^*)^{3/2}}{h^3}\sqrt{E_v - E}, \tag{2.19}$$

which is valid for $E \leq E_v$. From Eq. 2.16, Eq. 2.17, Eq.2.18, and Eq. 2.19, the distribution of electrons can be written as

$$n(E) = g_c(E)f(E), \tag{2.20}$$

and the distribution of holes can be written as

$$p(E) = g_v(E)(1 - f(E)). \tag{2.21}$$

To find the concentration of electrons in a semiconductor, Eq. 2.20 must be integrated over all energies above the conduction band,

$$n_0(E) = \int_{E_c}^{\infty} g_c(E)f(E)dE. \tag{2.22}$$

This integration will lead to the thermal-equilibrium electron concentration to be

$$n_0(E) = N_c exp(\frac{-(E_c - E_F)}{k_B T}), \tag{2.23}$$

where E_F is the fermi energy level and N_c is the effective density of states function in the conduction band,

$$N_c = 2(\frac{2\pi m_e^* k_B T}{h^2})^{3/2}. \tag{2.24}$$

A similar procedure is done to find the thermal-equilibrium hole concentration, Eq. 2.21 must be integrated over all energies below the valence band,

$$p_0(E) = \int_{-\infty}^{E_v} g_v(E)(1 - f(E))dE. \tag{2.25}$$

This integration leads to

$$n_0(E) = N_p exp(\frac{-(E_F - E_v)}{k_B T}), \tag{2.26}$$

where N_v is the effective density of states function in the valence band,

$$N_v = 2(\frac{2\pi m_h^* K_B T}{h^2})^{3/2}. \tag{2.27}$$

2.3.1 Intrinsic Carrier Concentration

An intrinsic semiconductor has the same number of electrons and holes, meaning all of the electrons in the conduction band have been excited from the valence band leaving a vacancy, or hole. This is otherwise known as an undoped semiconductor, such that no carriers have been introduced to the semiconductor from impurities or dopants. In this case, the intrinsic carrier density squared can be written as

$$n_i^2 = N_c N_v exp(\frac{E_g}{k_B T}). \tag{2.28}$$

Or otherwise written as

$$n_i^2 = np. \tag{2.29}$$

2.3.2 Extrinsic Carrier Concentration

An extrinsic semiconductor contains dopant atoms, either electron or hole contributors, that perturb the semiconductor from its intrinsic state. These dopant atoms will

create electron and hole concentrations that are different then the intrinsic carrier density. From Eq. 2.28 the intrinsic carrier density is written as

$$n_i^2 = n_0 p_0. \tag{2.30}$$

This fairly simple equation plays a large role in the fundamental physics of semiconductors.

2.3.3 Excess Carrier Concentration

For a semiconductor with carriers excited into the conduction band the electron carrier density is described as

$$n = n_0 + \Delta n, \tag{2.31}$$

where Δn is the excess carrier density. Assuming that $\Delta n = \Delta p$ (it is assumed that electron-hole pairs are created), the hole concentration is described as

$$p = p_0 + \Delta n. \tag{2.32}$$

2.4 Carrier recombination

As we have seen in the previous sections, electron-hole pairs can be excited by many different events. The particular excitation of interest here is absorption of a photon causing an electron to be excited to the conduction band, thus, creating an electron-hole pair. Once excited into an above ground state, the excited pair will have a

certain lifetime, or recombination rate, before the electron recombines with a hole. This mechanism is known as the recombination process and results in a recombination rate, or carrier lifetime. There are three main categories of recombination processes; Shockley-Read-Hall (SRH) recombination, radiative recombination, and Auger recombination [3], [4]. The instantaneous recombination rate takes all three of these mechanisms into account and is expressed as

$$R = R_{SRH} + R_{rad} + R_{Auger}, \tag{2.33}$$

where R_{SRH} is the SRH recombination term, R_{rad} is the radiative recombination term, and R_{Auger} is the Auger recombination term. These mechanisms will be discussed in the following section. The relation of the carrier density to recombination is expressed as

$$\frac{d\Delta n}{dt} = \frac{d\Delta p}{dt} = -R = -\frac{\Delta n}{\tau}, \tag{2.34}$$

where τ is the instantaneous carrier lifetime. The lifetime is a function of other parameters, such as Δn. The derivation of these equations will be addressed in Chap. 3. The lifetime of each individual recombination mechanism is expressed as

$$\tau^{-1} = \frac{R}{\Delta n}, \tag{2.35}$$

Another well known recombination process is surface recombination, however this is more related to device physics and will not be discussed in detail here.

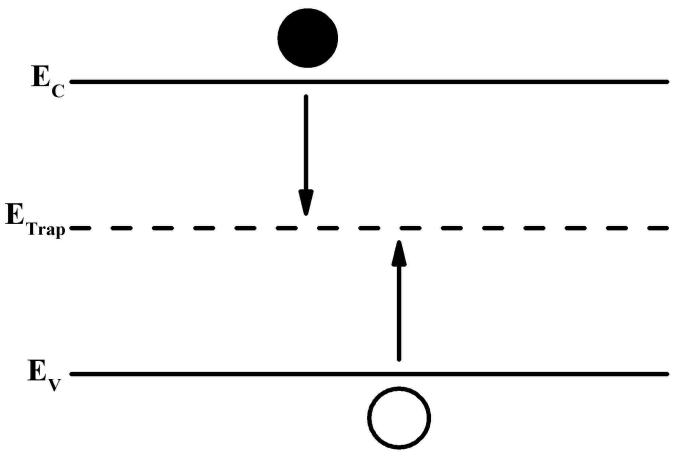

Figure 2.5: Shockley-Read-Hall recombination process. The electron and hole are captured by a trap state.

2.4.1 Shockley-Read-Hall Recombination

SRH recombination takes place through the capture of one carrier, either an electron or hole, via recombination centers. These recombination centers are due to impurities (i.e. defects in the crystal) and the density of centers is dependent on the density of impurities, meaning the higher quality of material the lower number of recombination centers. The recombination center energy level will sit within the bandgap energy of the semiconductor. Four different processes can occur from the recombination center, an electron can be trapped, an electron can be emitted, a hole can be trapped (resulting in an elimination of the electron-hole pair), or a hole can be emitted. An electron can only be captured by the trap if the defect does not already have an electron occupying it. A hole can only be captured if the trap state is occupied by an electron. An example of the SRH recombination process is shown in Fig. 2.5.

The SRH recombination rate is [3]

$$R_{SRH} = \frac{\sigma_h \sigma_e \nu_{th} N_t (np - n_i^2)}{\sigma_e (n + n_i e^{\frac{E_t - E_i}{k_B T}}) + \sigma_h (p + n_i e^{\frac{E_i - E_t}{k_B T}})}, \tag{2.36}$$

where ν_{th} is the thermal velocity of an electron, σ_e and σ_h are the capture cross sections of the recombination center for electrons and holes, N_T is the concentration of recombination centers, and E_T is the energy of the trap level. Dividing Eq. 2.36 by $\sigma_h \sigma_e \nu_{th} N_T$ with the following definition of the SRH lifetime for electrons

$$\tau_{e_0}^{-1} = \nu_{th} \sigma_e N_T, \tag{2.37}$$

and for holes,

$$\tau_{h_0}^{-1} = \nu_{th} \sigma_h N_T, \tag{2.38}$$

the SRH recombination can be described with associated electron and hole lifetimes as

$$R_{SRH} = \frac{np - n_i^2}{\tau_{h_0}(n_0 + \Delta n + n_i e^{\frac{E_t - E_i}{k_B T}}) + \tau_{e_0}(p_0 + \Delta n + n_i e^{\frac{E_i - E_t}{k_B T}})}. \tag{2.39}$$

For an n-type material ($n_0 \gg p_0$), Eq. 2.39 can be simplified to

$$R_{SRH} = \frac{\Delta n n_0 + \Delta n^2}{\tau_{h_0}(n_0 + \Delta n) + \tau_{e_0}(\Delta n)}. \tag{2.40}$$

The majority of material analyzed in this dissertation is doped n-type, therefore Eq. 2.41 will be the standard SRH recombination hereon. From Eq. 2.35 the SRH lifetime of an n-type semiconductor with a trap energy level near mid-bandgap is

expressed as

$$\tau_{SRH}^{-1} = \frac{n_0 + \Delta n}{\tau_{h_0}(n_0 + \Delta n) + \tau_{e_0}(\Delta n)}. \tag{2.41}$$

In the case of low-injection, $n_0 \gg \Delta n$, $\tau_{SRH} = \tau_{h_0}$, meaning all of the trap centers are occupied by an electron leaving the SRH hole lifetime as the limiting factor. For high injection, $\Delta n \gg n_0$, the SRH electron lifetime will be the limited mechanism ($\tau_{SRH} = \tau_{e_0}$).

2.4.2 Radiative Recombination

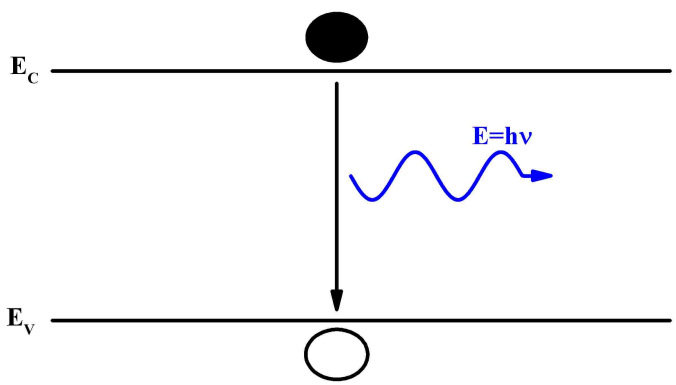

Figure 2.6: Radiative recombination process. The electron recombines with a hole in the valence band, emitting a photon.

Radiative recombination is due to the recombination of an electron and hole which results in the emission of a photon, as shown in Fig. 2.6. The rate of radiative recombination is described as [4]

$$R_{rad} = B(np - n_i^2), \tag{2.42}$$

where B is the radiative recombination coefficient. For n-type material, Eq. 2.42 can

be simplified to

$$R_{rad} = B(\Delta n n_0 + \Delta n^2). \tag{2.43}$$

The radiative lifetime for n-type material is described as

$$\tau_{rad}^{-1} = B(n_0 + \Delta n). \tag{2.44}$$

In the case of a direct-gap semiconductor, the radiative recombination rate can be calculated by

$$B = \frac{1}{n_i^2 c^2 \hbar^3} \int_0^{\inf} \frac{\epsilon(E_\lambda)\alpha(E_\lambda)E_\lambda^2}{e^{E_\lambda/k_B T} - 1} dE, \tag{2.45}$$

where ϵ is the permittivity and α is the optical absorption, which for a direct-gap semiconductor with parabolic bands has the form [5]

$$\alpha_{direct} = \frac{2^{3/2}}{3\mu} \frac{m_0 e^2}{\hbar^2} [\frac{m_e m_h}{m_0(m_e + m_h)}]^{3/2} (1 + \frac{m_0}{m_e} + \frac{m_0}{m_h})(\frac{E_\lambda - E_g}{m_0 c^2})^{1/2}, \tag{2.46}$$

where E is the photon energy and μ is the index of refraction. Combining Eq. 2.45 and Eq. 2.46 the radiative recombination can be found as [4]

$$B = \frac{(2\pi)^{3/2}}{3} \frac{\hbar e^2}{m_0^2 c^2} \mu (\frac{m_0}{m_e + m_h})^{3/2} (1 + \frac{m_0}{m_e} + \frac{m_0}{m_h}) \frac{E_g^2}{(k_B T)^{3/2} (m_0 c^2)^{1/2}}, \tag{2.47}$$

The major take away from Eq. 2.47 is that as $T \to 0$ the radiative lifetime will approach zero. As the temperature rises from zero, the lifetime will have a $E_g^2/T^{3/2}$ dependence until eventually intrinsic effects dominate. However, in physical semiconductors Auger recombination will begin to dominate at these high temperatures, resulting in a lesser carrier lifetime than that of the radiative.

2.4.3 Auger Recombination

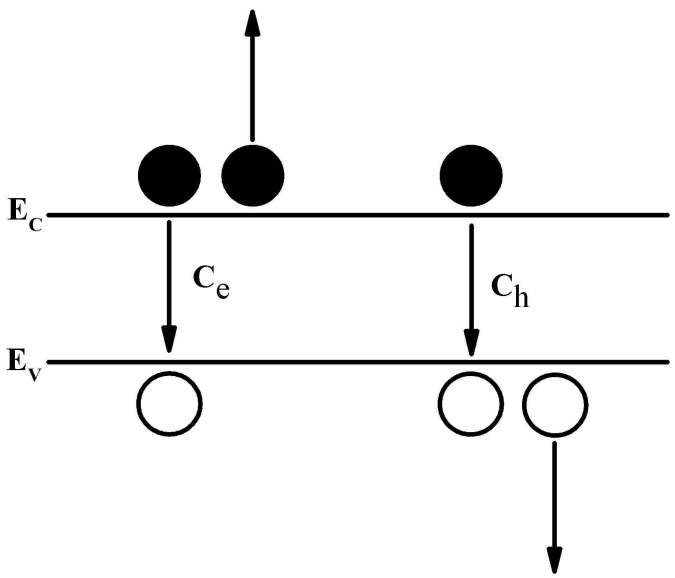

Figure 2.7: Auger recombination process. The Auger-1 process is shown on the left which includes two electrons and one hole. The Auger-7 process is depicted on the right which includes two holes and one electron.

An Auger recombination process is a three-body process that requires either two electrons and one hole or two holes and one electron plus the emission or absorption of a phonon, therefore this is a nonradiative process. These processes can be seen in Fig. 2.7. The Auger 1 process is dependent on two electrons and one hole and the Auger 7 is dependent on 2 holes and one electron. For the Auger 1 process, the band-to-band Auger recombination process is characterized by the coefficient [6]–[9]

$$C_n = \frac{8(2\pi)^{5/2} e^4 m_0}{\hbar^3} \frac{(m_e/m_0)|F_1F_2|^2 n_0 (k_B T/E_g)^{3/2}}{\epsilon_0^{\inf}(1+\mu)^{1/2}(1+2\mu)} \times e^{-\frac{1+2\mu}{1+\mu}\frac{Eg}{k_B/T}}, \tag{2.48}$$

where $\mu = m_e/m_h$, $\epsilon_{\inf}$ is the high frequency dielectric constant, $|F_1F_2|$ is the Bloch function overlap between states involved in the recombination, or scattering, process.

For intrinsic material, relatively small values of Δn, the Auger lifetime reduces to [6], [9]

$$\tau^{i}_{Auger} \approx \frac{n_i}{2C_n} \tag{2.49}$$

For the Auger 7 process, which includes an electron recombining with a hole resulting in the energy exciting a hole from the light-hole band to the heavy-hole band, can be related to the Auger 1 process by [10]

$$R_{A_7} = \frac{R_{A_7}}{\gamma}\frac{n}{p}, \tag{2.50}$$

where γ is dimensionless constant. The total Auger recombination rate is written as

$$R_{Auger} = C_n(np - n_i^2)n + C_h(np - n_i^2)p. \tag{2.51}$$

From Eq. 2.51 the Auger lifetime can be written as

$$\tau^{-1}_{Auger} = \frac{C_n(np - n_i^2)n + C_p(np - n_i^2)p}{\Delta n} \tag{2.52}$$

Eq. 2.52 can then be simplified to

$$\tau^{-1}_{Auger} = C_n(n_0 + p_0 + \Delta n)n + C_p(n_0 + p_0 + \Delta n)p. \tag{2.53}$$

The two scenarios of most interest are large n-type doping, $n_0 \gg \Delta n$, and high-injection levels, $\Delta n \gg n_0$. In the case of large doping the n_0 term will dominate, and the Auger lifetime will take the from

$$\tau^{-1}_{Auger} \approx C_n n_0^2. \tag{2.54}$$

For high-injection levels the Δn term will dominate and Auger lifetime will take the form

$$\tau_{Auger}^{-1} \approx C_n \Delta n^2 + C_p \Delta n^2. \tag{2.55}$$

Therefore, to correctly determine the influence of Auger recombination in a material,

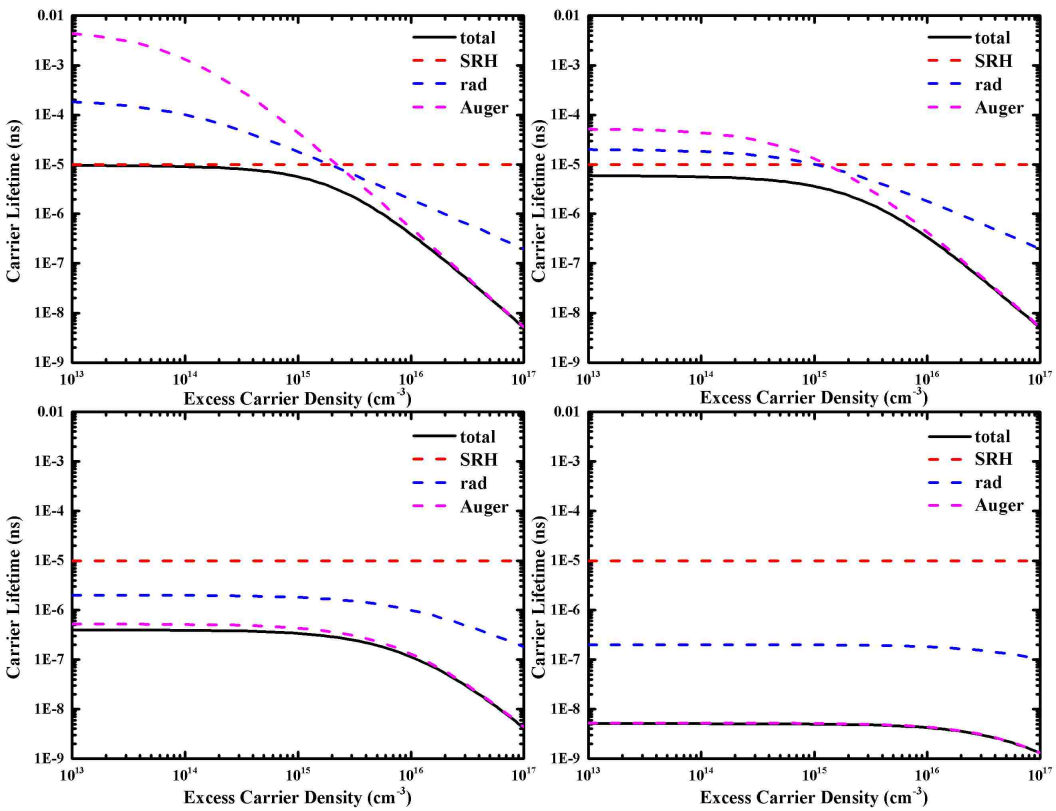

Figure 2.8: Simulated carrier lifetime as a function of excess carrier density for samples of varying electron doping using published values of MWIR InAs/InAsSb T2SL [11]. The recombination parameters used were $A^{-1} = 10\mu$s, $B_r = 1 \times 10^{-10}$ cm^{3}s^{-1}, and $C_n = 1.9 \times 10^{-26}$ cm^{6}s^{-1}. The doping values used were $n_0 = 1 \times 10^{14}$ cm^{-3} (upper left), $n_0 = 1 \times 10^{15}$ cm^{-3} (upper right), $n_0 = 1 \times 10^{16}$ cm^{-3} (lower left), and $n_0 = 1 \times 10^{17}$ cm^{-3} (lower right).

information on C_n and C_p must be known. To analyze these two components, studies

of minority carrier lifetime of samples with varying doping density (n_0 and p_0) have been performed on various samples [12]–[16]. However, information for Auger hole recombination (C_p) in InAs/InAsSb T2SLs is lacking. Therefore, in this dissertation it is assumed that $\gamma \to \inf$, meaning the Auger recombination is entirely due to the Auger 1 process. With this assumption Eq. 2.53 is simplified to

$$\tau_{Auger}^{-1} \approx C_n(n_0 + \Delta n)^2. \tag{2.56}$$

2.4.4 Total carrier recombination

The total carrier lifetime of a semiconductor takes each recombination mechanism into account and can be written as

$$\tau^{-1}(n) = \tau_{SRH}^{-1} + \tau_{rad}^{-1} + \tau_{Auger}^{-1} \tag{2.57}$$

From equations Eq.2.39, Eq. 2.44, and Eq. 2.55, Eq. 2.57 can be expanded as

$$\tau^{-1}(\Delta n) = \frac{n_0 + \Delta n}{\tau_{h_0}(n_0 + \Delta n) + \tau_{e_0}(\Delta n)} + B(n_0 + p_0 + \Delta n) + C_n(n_0 + p_0 + \Delta n)^2. \tag{2.58}$$

In the case of an n-type doped material, Eq. 2.58 can be simplified to

$$\tau^{-1} = \frac{n_0 + \Delta n}{\tau_{h_0}(n_0 + \Delta n) + \tau_{e_0}(\Delta n)} + B(n_0 + \Delta n) + C_n(n_0 + \Delta n)^2. \tag{2.59}$$

Solving for the minority carrier lifetime, or the low-injection limit ($\Delta n \to 0$), Eq. 2.59 is simplified to

$$\tau_{MC}^{-1} = \tau_{h_0}^{-1} + Bn_0 + C_n n_0^2. \tag{2.60}$$

From Eq. 2.59 and Eq. 2.60, it can be seen that, in general, the carrier lifetime will have three different regimes; the very high-injection regime ($\Delta n \gg n_0$), the moderate high-injection regime ($\Delta n \approx n_0$), and the low-injection regime, also known as the minority carrier regime, ($\Delta n \to 0$). The very high-injection regime is most-likely dominated by Auger recombination as this is dependent on the excess carrier density squared (Δn^2). Recombination in the moderate high-injection and minority carrier regime will be dependent on many different factors depending on the doping and recombination mechanisms. These factors are more easily explained by curves pertaining to different material parameters.

Fig.2.8 shows the carrier lifetime as a function of excess carrier density for a InAs/InAsSb T2SL at 100 K, with recombination characteristics from Ref. [11]. The recombination parameters used were $A^{-1} = 10\mu s$, $B_r = 1 \times 10^{-10} cm^3 s^{-1}$, and $C_n = 1.9 \times 10^{-26} cm^6 s^{-1}$. The upper-left plot resembles a partially doped sample, $n_0 = 1 \times 10^{14} cm^{-3}$, a level that would represent a not-intentionally-doped (nid) sample. For this doping density the minority carrier lifetime is limited by SRH recombination and the high-injection regime is dominated by Auger recombination. At the excess carrier density of $1 \times 10^{15} cm^{-3}$, the lifetime is partially limited by each recombination mechanism. This could lead to difficulties of accurately measuring the radiative recombination mechanism. The upper-right plot represents the lifetime characteristics of a slightly-doped sample, $n_0 = 1 \times 10^{15} cm^{-3}$. The minority carrier lifetime in this scenario comprised of all three recombination mechanisms with SRH recombination making the greatest impact. The lower plots are for a moderately doped sample, $n_0 = 1 \times 10^{16} cm^{-3}$, and highly-doped sample, $n_0 = 1 \times 10^{17} cm^{-3}$. For these doping levels the carrier lifetime is limited by Auger recombination in both

the minority carrier and high-injections regimes. These examples resemble physical measurements that will be shown in the following chapter.

2.5 References

[1] D. Neamen, *Semiconductor Physics and Devices: Basic Principles, Third Edition*, E. A. Jones, Ed. McGraw-Hill, 2003, ISBN: 0-07-232107-5.

[2] R. de L. Kronig and W. G. Penney, "Quantum mechanics of electrons in crystal lattices," *Proceedings of the Royal Society of London A: Mathematical, Physical and Engineering Sciences*, vol. 130, no. 814, pp. 499–513, 1931, ISSN: 0950-1207. DOI: 10.1098/rspa.1931.0019. eprint: http://rspa.royalsocietypublishing.org/content/130/814/499.full.pdf. [Online]. Available: http://rspa.royalsocietypublishing.org/content/130/814/499.

[3] W. Shockley and W. T. Read, "Statistics of the recombination of holes and electrons," *Phys. Rev.*, vol. 87, pp. 835–842, 1952.

[4] R. N. Hall, "Recombination processes in semicondcutors," *Proc. of IEE*, vol. 106, pp. 923–931, 1959.

[5] J. Bardeen, F. J. Blatt, and L. H. Hall, "Indirect transitions form the valence to the conduction bands," in *Photoconductivity Conference*, John Wiley, 1956, p. 146.

[6] A. R. Beattie and P. T. Landsberg, "Auger effect in semiconductors," *Proc. of Royal Soc.*, vol. 249, pp. 16–29, 1959.

[7] J. Blakemore, *Semiconductor Statistics*. Mineola, New York: Dover Publications, Inc., 1962.

[8] V. C. Lopes, A. J. Syllaios, and M. C. Chen, "Minority carrier lifetime in mercury cadmium telluride," *Semicond. Sci. Technol.*, vol. 8, p. 824, 1993.

[9] B. V. Olson, "Time-resolved measurements of charge carrier dynamics and optical nonlinearities in narrow-bandgap semiconductors," PhD thesis, University of Iowa, 2013.

[10] C. M. Ciesla, B. N. Murdin, T. J. Phillips, A. M. White, A. R. Beattie, C. J.G. M. Landerak, C. T. Elliot, C. R. Pidgeon, and S. Sivananthan, "Auger recombination dynamics of $Hg_0.795Cd_0.205Te$ in the high excitation regime," *Appl. Phys. Lett.*, vol. 71, pp. 491–493, 1997.

[11] Y. Aytac, B. V. Olson, J. K. Kim, E. A. Shaner, S. D. Hawkins, J. F. Klem, M. E. Flatt, and T. F. Boggess, "Effects of layer thickness and alloy composition on carrier lifetimes in mid-wave infrared inas/inassb superlattices," *Applied Physics Letters*, vol. 105, no. 2, 022107, 2014. DOI: `http://dx.doi.org/10.1063/1.4890578`. [Online]. Available: `http://scitation.aip.org/content/aip/journal/apl/105/2/10.1063/1.4890578`.

[12] C. H. Grein, P. M. Young, and H. Ehrenreich, "Minority carrier lifetimes in ideal InGaSb/InAs superlattices," *Appl. Phys. Lett.*, vol. 61, pp. 2905–2907, 1992.

[13] M. E. Flatté, C. H. Grein, T. C. Hasenberg, S. A. Anson, D.-J. Jang, J. T. Olesberg, and T. F. Boggess, "Carrier recombination rates in narrow-gap $InAs/Ga_{1-x}In_xSb$-based superlattices," *Phys. Rev. B*, vol. 59, pp. 5745–5750, 1999.

[14] C. H. Grein, M. E. Flatté, J. T. Olesberg, S. A. Anson, L. Zhang, and T. F. Boggess, "Auger recombination in narrow-gap semiconductor superlattices incorporation antimony," *J. Appl. Phys.*, vol. 92, pp. 7311–7316, 2002.

[15] S. Anikeev, D. Donetsky, G. Belenky, S. Luryi, C. A. Wang, J. M. Borrego, and G. Nichols, "Measurement of the auger recombination rate in p-type 0.54 eV GaInAsSb by time-resolved photoluminescence," *Appl. Phys. Lett.*, vol. 83, p. 3317, 2003.

[16] C. H. Grein, P. M. Young, M. E. Flatté, and H. Ehrenreich, "Long wavelength InAs/InGaSb infrared detectors: Optimization of carrier lifetimes," *J. Appl. Phys.*, vol. 78, pp. 7143–7152, 1995.

Chapter 3

Carrier lifetime measurement techniques

Carrier lifetime analysis can provide vital information on the quality of semiconductor material and how well that material will perform in use for specific applications. For example, the minority carrier lifetime can be directly related to dark-diffusion currents in a photodetector [1], [2] and other minority-carrier devices. There are many different carrier lifetime measurement techniques. For a direct-gap semiconductor, measurement of photoluminescence has generally been the most practical and straightforward. However, as the bandgap energy of the semiconductor is reduced, or the wavelength of emitted photoluminescence is increased, the detectivity of detectors associated with sensing that emission decrease, thus, limiting capabilities. For example, performing photoluminescence measurements on GaAs is easily accomplished do to the availability of highly sensitive detectors [3]. Whereas, performing the identical measurements on material with MWIR and LWIR bandgap

energy becomes increasingly hard due to the reduction in photodetectors. A more universal approach to measuring the lifetime is monitoring change in conductance of the sample using a microwave radiation probe. The purpose of this chapter is to provide background and examples of various lifetime techniques, along with some discussion of pros and cons of each approach.

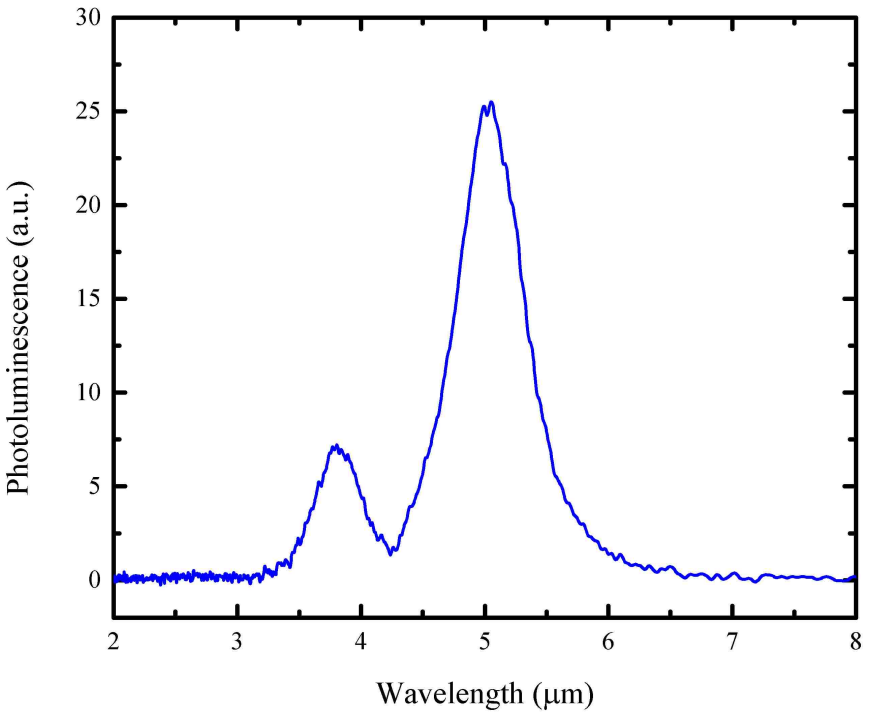

Figure 3.1: Photoluminescence spectra from a MWIR InAs/InAsSb T2SL at 100 K. The 5.03 μm and 3.79 μm peaks correspond to the InAs/InAsSb superlattice and InAsSb lattice matched to GaSb cap, respectively.

Initial efforts were focused on photoluminescence measurements. As material quality has improved, these lifetime measurement techniques have transitioned to microwave reflectance measurements. For comparison, a MWIR InAs/$InAs_{0.66}Sb_{0.34}$ T2SL was measured by each lifetime measurement technique described in the following sections. The sample is grown using molecular beam epitaxy on a 3 inch n-type

doped GaSb substrate with a (100) orientation. The sample consists of a barrier region, the T2SL, a second barrier region, and an InAsSb lattice matched to GaSb cap. The barrier regions help confine carriers generated in the T2SL to help limit recombination to the T2SL. The T2SL region consists of 750 periods of unintentionally doped 4.07 nm InAs/ 1.29 $InAs_{0.66}Sb_{0.34}$. The T2SL bandgap energy was approximately 5 μm. The bandgap was found by photoluminescence measurements, shown in Fig. 3.1. The photoluminescence measurement consisted of a modulated 785 nm laser to inject carriers in the sample and a step-scan Jasco 6300 FTIR to measure the spectral response of the emitted photoluminescence. The photoluminescence spectra is shown in Fig. 3.1, the 5.03 μm and 3.79 μm peaks correspond to the InAs/InAsSb superlattice and InAsSb lattice matched to GaSb cap, respectively.

3.1 Rate Equation

The temporal differential equation relating the carrier density to generation, recombination, and diffusion is known as the time-dependent drift diffusion equation and is expressed as

$$\frac{\partial \Delta n(x,t)}{\partial t} = G(t) + D\nabla^2 \Delta n(x,t) - \frac{\Delta n(x,t)}{\tau}, \tag{3.1}$$

where G is the generation term and D is the minority electron diffusivity. Making the assumption that the temporal and spatial variables of excess carrier density can separated, the excess carrier density can then be described as

$$\Delta n(x,t) = f(t)g(x). \tag{3.2}$$

Substituting Eq. 3.2 into Eq. 3.1 and combining like terms, the diffusion equation becomes

$$\frac{1}{f(t)}\frac{df(t)}{dt} + \frac{1}{\tau} - G(t) = D\frac{\nabla^2 g(x)}{g(x)} = C, \tag{3.3}$$

where the left-hand side of the equation contains the time dependent terms and the right-hand side contains the spatial terms. For the samples under test in this dissertation, it is assumed that the diffusion term is negligible due to the small diffusion of carriers in the unbiased device (flat-band). In other words, the ambipolar transport of carriers is small compared to the spot size of injected carriers, therefore diffusion does not have large impact on Eq. 3.1. The generation term is subject to the injected carriers. For a pulsed measurement, the generation term can be simplified to the impulse function. For steady-state measurements, the generation term will take the form of a time dependent equation. These two scenarios will be further expanded upon in the following sections.

From Eq. 2.35, the recombination term is given as

$$R = \frac{\Delta n}{\tau}, \tag{3.4}$$

where τ is the carrier lifetime. From Eq. 2.57, Eq. 3.4, and Eq. 3.1, the differential equation pertaining to carrier density is written as

$$\frac{d\Delta n}{dt} = G(t) - \Delta n[A + Bn + Cn^2], \tag{3.5}$$

where A represents the SRH lifetime ($A = \tau_{SRH}^{-1}$), B is the radiative recombination coefficient, and C is the Auger recombination coefficient. In the following sections, Eq. 3.5 will be used for explanation of particular measurement techniques, namely

time-resolved and frequency modulated approaches.

3.2 Time-resolved photoluminescence

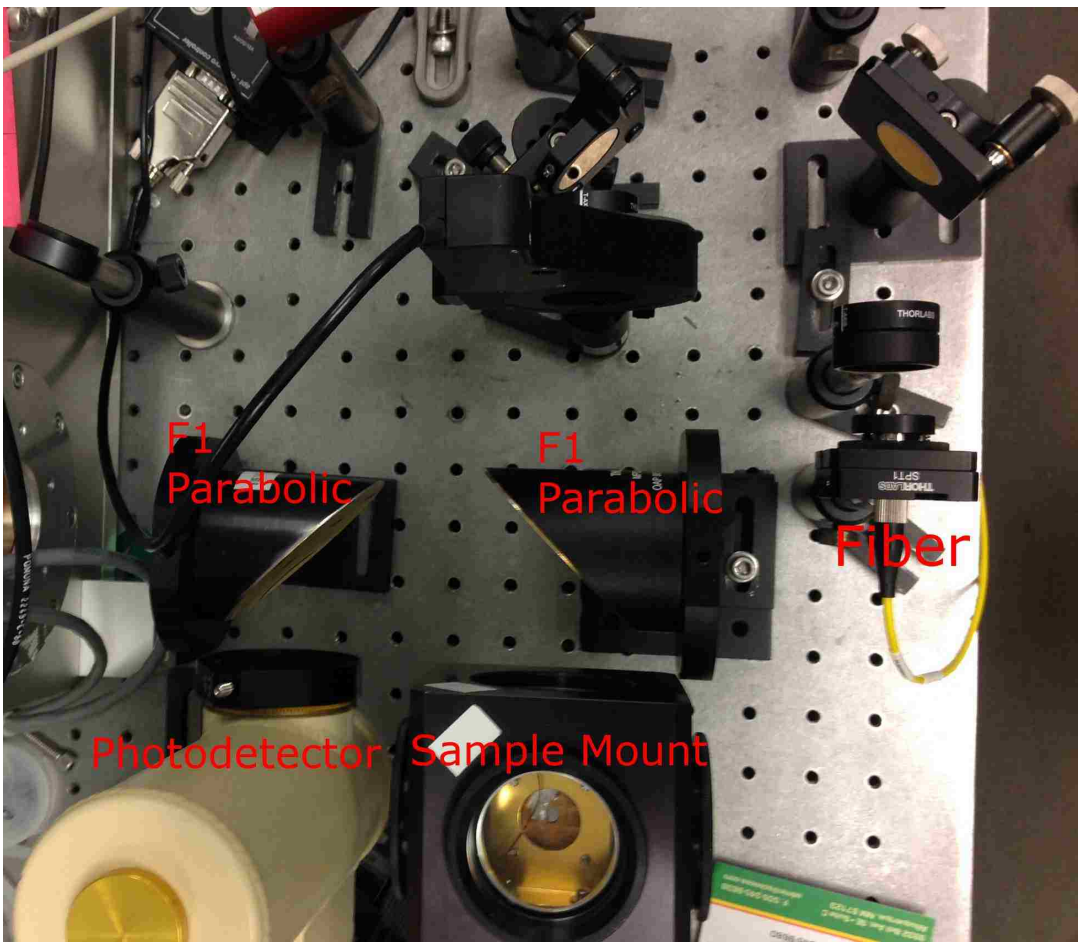

Figure 3.2: Basic setup of photoluminescence-based measurements, consisting of two F1 parabolic mirrors to collimate and focus the emission of the sample under test.

Time-resolved photoluminescence (TRPL) utilizes a pulsed laser to excite electron-hole pairs that then recombine. The recombination process will be dependent on the Shockley-Read-Hall, radiative, and Auger recombination, as described in the pre-

vious chapter. The carriers that radiatively recombine will emit photons. These photons are temporally measured using a photodetector of appropriate cutoff wavelength. The measured photoluminescence lifetime will be representative of the carrier lifetime. Generally, the pulse width of the excitation laser will be much smaller than the lifetime of the sample under test. If not, measurement of the carrier lifetime, in general, will be skewed, however it may still be possible to measure the minority carrier lifetime if the pulse width to lifetime ratio is small enough.

The photoluminescence intensity is described as [4]

$$I_{PL}(n) = B(np - n_i^2). \tag{3.6}$$

For an n-type material, Eq. 3.6 can be simplified to

$$I_{PL}(n) = B(\Delta n n_0 + \Delta n^2). \tag{3.7}$$

Eq. 3.7 shows two distinct regions of photoluminescence dependence on excess carrier density, above and below the doping level. The significance of this can be better expressed by assuming that the excess carrier density will have a temporal exponential decay such that

$$I_{PL}(t) = B(n_0 \Delta n e^{\frac{t}{\tau}} + \Delta n^2 e^{\frac{2t}{\tau}}). \tag{3.8}$$

Due to the non-linear dependence, for injected carrier densities near and greater than the doping density, the measured response will be proportional to the actual carrier lifetime. Therefore, a calibration of the injected carrier density to photoluminescence signal must be performed. Although this was not performed for TRPL measurements in this dissertation, a thorough explanation of the calibration method is shown in the

Chap. 3.4. Although it is possible to measure the higher order recombination terms using TRPL, the most straightforward use is for measurement the minority carrier lifetime. To obtain the minority carrier lifetime you may inject carriers at levels less than the background doping, resulting in measurements directly relating to the minority carrier lifetime of the material. Another option is to fit the tail of the decay, however, this becomes a somewhat arbitrary practice, therefore decreasing the pump excitation to the point of single exponential decay is the best practice for obtaining the minority carrier lifetime. For low-doped materials, injecting carriers at these low levels while maintaining sufficient signal to noise becomes quite challenging.

For a more thorough explanation of the photoluminescence signal dependence on excess carrier density, Eq. 3.7 and Eq. 3.5 were numerically solved using recombination characteristics based on published InAs/InAsSb T2SL recombination [5]. For pulsed excitation, assuming impulse response of injected carriers, Eq. 3.5 can be written as

$$\frac{d\Delta n}{dt} = -\Delta n[A + Bn + Cn^2], \tag{3.9}$$

where the initial condition of the differential equation is set to the injected carrier density (i.e. $n(t = 0) = n_{inj} = \Delta n(t = 0)$). The numerical solution to Eq. 3.9 provides the temporal response of the carrier density for a given injected carrier density. For this example the recombination parameters used were $A^{-1} = 5\mu s$, $B = 1 \times 10^{-11} cm^3 s^{-1}$, and $C = 1.5 \times 10^{-26} cm^6 s^{-1}$ and the doping density of the sample was set to $n_0 = 1 \times 10^{15} cm^{-3}$ Fig. 3.3 shows the temporal response of the excess carrier density found from numerically solving Eq. 3.9 for an injected carrier density of $1 \times 10^{17} cm^{-3}$. To show non-linear correlation between excess carrier density and photoluminescence, the time derivative of the photoluminescence intensity,

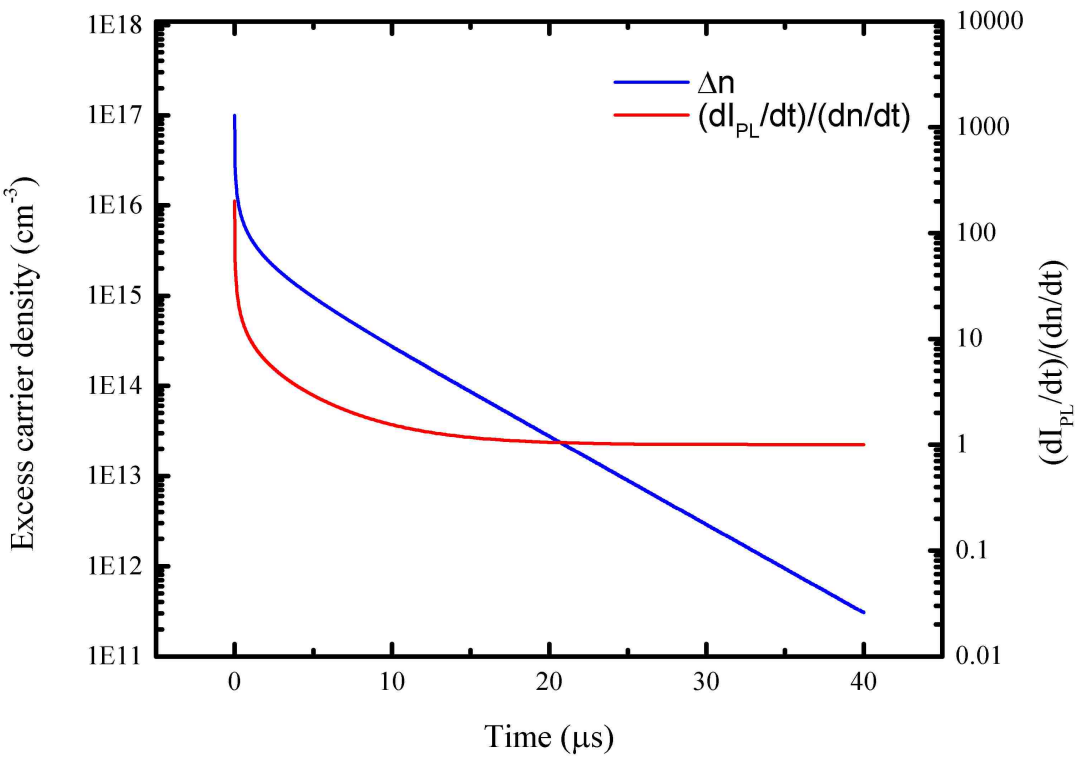

Figure 3.3: Time-resolved photoluminescence of an InAs/InAsSb MWIR T2SL at a temperature of 100 K, black curve. The dashed-red curve is an exponential fit to the tail of the photoluminescence decay.

$B(d\Delta n n_0 + \Delta n^2)/dt$, divided by the time derivative of the carrier density, $d\Delta n/dt$, is also shown. From where the quotient 1, the temporal position were the photoluminescence decay directly represents the carrier lifetime is approximately 20 μs. This position corresponds to an excess carrier density of $3 \times 10^{13} cm^{-3}$. Reaching injected carrier density this low while maintaining photoluminescence signal becomes extremely challenging. For comparison to other techniques, the minority carrier lifetime of a MWIR InAs/InAsSb T2SL was measured using TRPL. The setup consisted of two F1 parabolic mirrors, the first to collimate and the second to focus the photoluminescence from the sample, a cryogenically cooled InSb detector to sense the

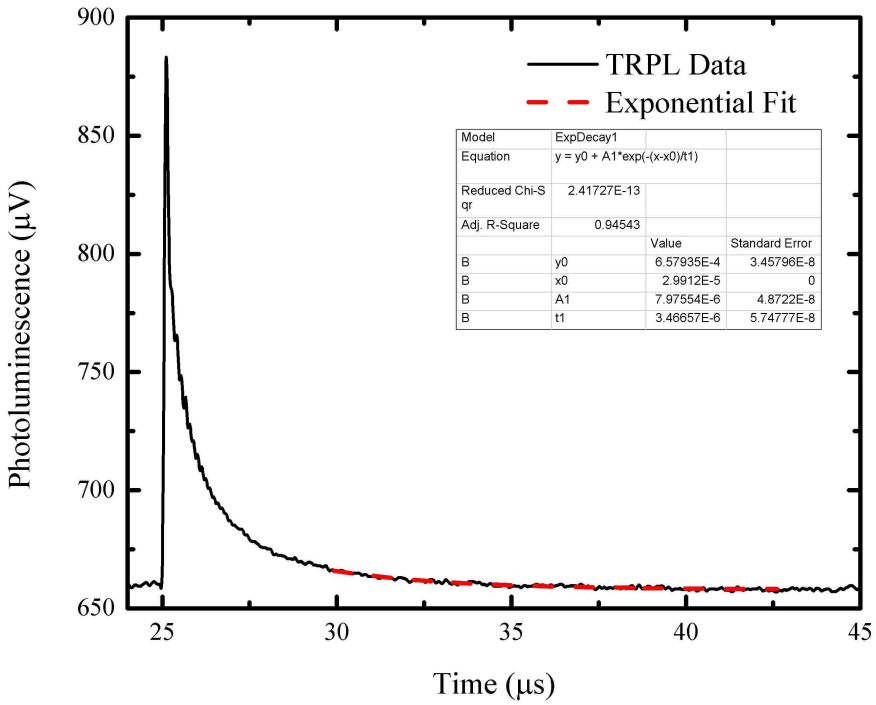

Figure 3.4: Time-resolved photoluminescence of an InAs/InAsSb MWIR T2SL at a temperature of 100 K, black curve. The dashed-red curve is an exponential fit to the tail of the photoluminescence decay.

emitted photoluminescence, and a 1535 nm pulsed laser to optically inject carriers in the sample. This laser wavelength will also inject carriers in the cap, however the lifetime of the cap is on the order of 100 ns and will not influence the minority carrier lifetime of the T2SL. A 2.4 μm longpass filter was used to block the pump beam from the InSb detector. The photoluminescence decay is shown in Fig. 3.4. An exponential fit to the tail of the photoluminescence decay is used to find the minority carrier lifetime of the T2SL. A minority carrier lifetime 3.47μs is found.

3.3 Frequency modulated photoluminescence

Frequency modulated photoluminescence (FMPL) utilizes steady-sate carrier generation with small-signal modulation to investigate the carrier lifetime at specific carrier densities. For FMPL, the generation term is written as

$$G = G_{DC} + G_{AC}\cos(\omega t), \tag{3.10}$$

where G_{DC} is the steady-state generation value and G_{AC} is the frequency modulated term. Inserting Eq. 3.10 in Eq. 3.1 where the recombination term is denoted by Eq. 3.4 gives

$$\frac{d\Delta n}{dt} = G_{DC} + G_{AC}\cos(\omega t) - \frac{\Delta n}{\tau}, \tag{3.11}$$

where τ is the carrier lifetime. Eq. 3.11 is the common description of the differential equation pertaining to carrier density of the FMPL method. Assuming τ is a constant, the equation can be analytically solved giving

$$\Delta n(t) = \tau G_{DC} + \tau\frac{G_{AC}}{\sqrt{1+\tau^2\omega^2}}\cos(\omega t - \phi), \tag{3.12}$$

where $\phi = \arctan(1/\tau\omega)$. From this equation it is seen that the modulated excess carrier density term will be dependent on the modulation frequency and carrier lifetime. The steady-state excess carrier density is dependent on the steady-state generation term and lifetime. Therefore, the carrier lifetime as a function of excess carrier density may be probed. The AC term of the photoluminescence intensity is

$$I_{PLAC} \propto \frac{\tau G_{AC}}{\sqrt{1+\tau^2\omega^2}}. \tag{3.13}$$

As the modulation frequency is swept, the AC term will begin to roll-off. From this roll-off the carrier lifetime at the specific steady-state carrier density may be either calculated or fit. Using the 3dB point of the AC roll-off, the carrier lifetime is found to be

$$\tau = \frac{1}{2\pi}\frac{\sqrt{3}}{f}, \tag{3.14}$$

where f is the modulation frequency. The steady-state carrier density is found from the product of the DC generation and carrier lifetime.

$$n_{DC} = \tau G_{DC}. \tag{3.15}$$

An example of data taken using this method is shown in Fig. 3.5. This data was taken using a 1625 nm laser as the pump. The photoluminescence was captured using two F1 parabolic mirrors to collimate emission and then focus onto a cryogenically cooled InSb detector. A 2.4 μm longpass filter was used to block the pump laser from the detector.

Although the signal to noise ratio of the FMPL method is increased by the reduction in the system bandwidth, measuring the lifetime of some lower doped samples ($n_0 \propto 10^{14} cm^{-3}$) has remained challenging. This method does, however, remain relevant for higher doped samples where the minority carrier lifetime can be resolved at higher steady-state carrier densities.

Another attribute of the frequency-modulated method is the assumption made to reach Eq. 3.11, which is the carrier lifetime is not dependent on carrier density. The full description of the carrier density using frequency modulated carrier generation

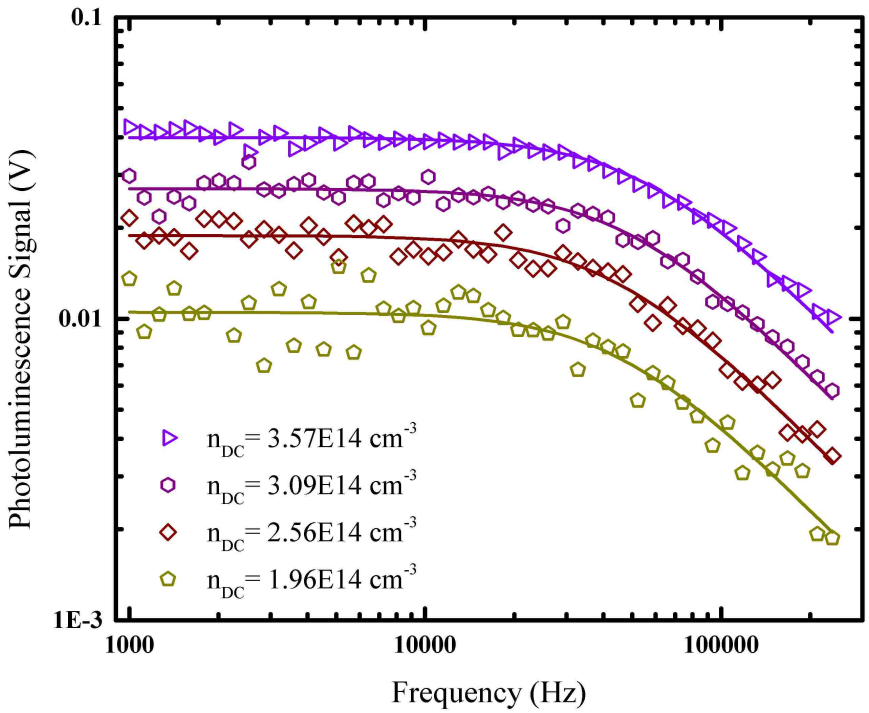

Figure 3.5: Frequency modulated photoluminescence data of the InAs/InAsSb T2SL sample for varying DC generation levels. The sample was cryogenically cooled to 100 K.

is

$$\frac{d\Delta n}{dt} = G_{DC} + G_{AC}\cos(\omega t) - \Delta n[A + Bn + Cn^2]. \tag{3.16}$$

This equation cannot be solved analytically and must be approached numerically. A quick observation of Eq 3.19 shows higher order terms pertaining to the carrier density term, which could lead to higher harmonic terms being generated from the single-frequency modulated generation term. Through numerical simulations it has been shown that for small-signal modulation ($G_{DC} \gg G_{AC}$) these higher harmonic terms do not play a large roll even when the steady-state carrier density is larger than the doping level. However, for large modulation ($G_{DC} \propto G_{AC}$) the higher order terms do affect the carrier density. These aspects are looked at in-depth in Chap. 4.

3.4 Carrier lifetime measurements via microwave reflectance

An alternative to photoluminescence-based lifetime measurements is to measure a change in conductivity by reflection of microwave radiation. This measurement technique is independent of the bandgap energy of the material under test. Therefore, it is a more versatile approach to measuring lifetime of material systems with largely varying bandgap energies, such as InAs/InAsSb T2SLs.

3.4.1 Time-resolved microwave reflectance

Similarly to TRPL, time-resolved microwave reflectance (TMR) utilizes a pulsed laser to excite electron hole pairs in the T2SL. The excess charge creates a change of conductivity of the T2SL, which results in a change in reflection of continuous-wave microwave radiation. Therefore, the recombination of charge carriers can be temporally monitored by measuring the change in power of reflected microwave radiation after optical excitation.

An advantage of TMR is the carrier lifetime decay curve is dependent on the excess carrier density and conductivity, whereas, for example, the photoluminescence decay curve has a squared dependence on excess carrier densities above doping levels (Eq. 3.6. This advantage makes measuring the minority carrier lifetime and higher-order recombination terms, such as Auger recombination, more straightforward. In order to resolve these recombination terms, a calibration of excess carrier density to signal level must be made.

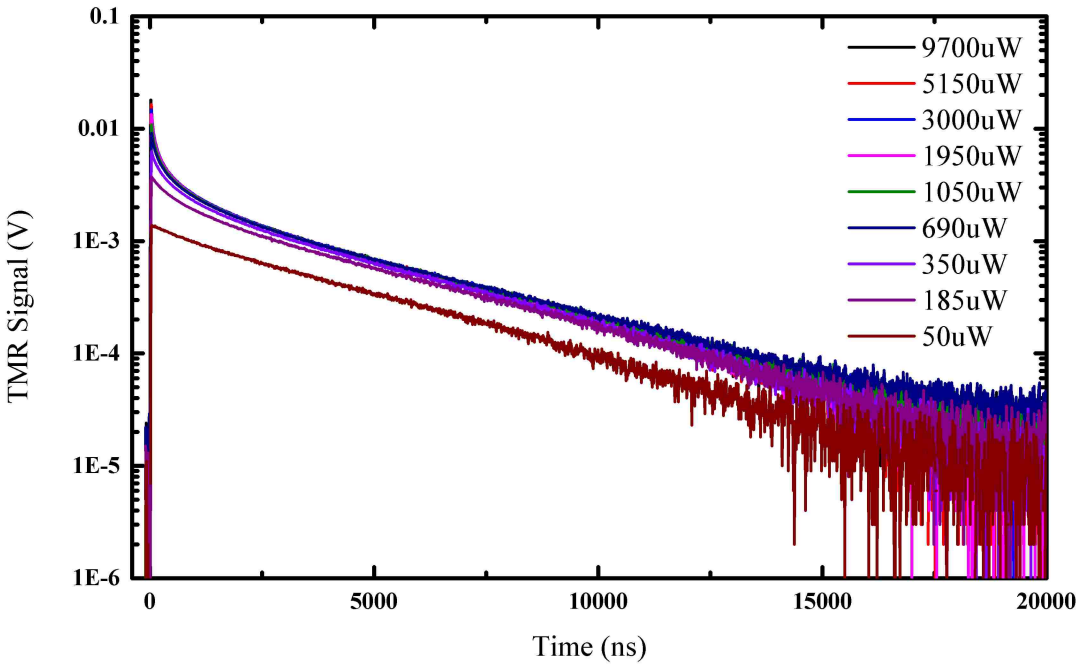

Figure 3.6: Time-resolved microwave reflectance of an InAs / InAsSb MWIR T2SL at a temperature of 100 K.

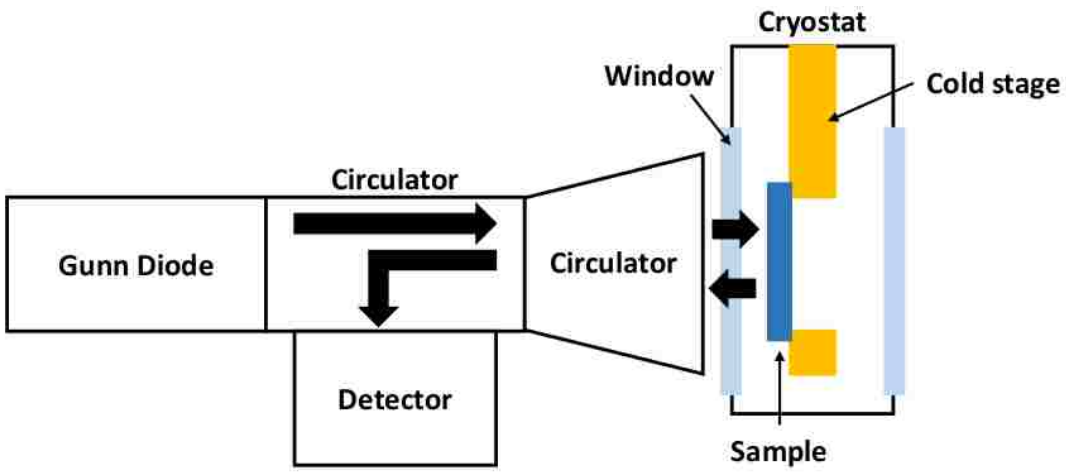

Figure 3.7: Block diagram of microwave apparatus used for time-resolved microwave reflectance and frequency-modulated conductance.

As an example for this section, a InAs/InAsSb MWIR T2SL sample is used for lifetime characterization via TMR, photoluminescence spectra shown in Fig. 3.1. The TMR setup consists of a tunable optical parametric oscillator which provides pulses of $5 - 10ns$ FWHM at a repetition rate of 1 kHz. The wavelength of choice for this measurement was $3.7\mu m$ to provide a relative uniform distribution of carriers in the absorber. At this wavelength the absorption coefficient of the T2SL absorber is approximately 3600 cm^{-1} [6]. The measured $1/e$ radius of the pump beam was $2.75mm$. The pump energy is controlled using a ZnSe polarizer. The pump beam illuminates the backside of the sample, because the substrate consists of n-type doped GaSb absorption at 3.7 μm is relatively low, roughly 10 cm^{-1}. A 94-GHz Gunn diode is used to source the continuous-wave microwave radiation and is directed to the sample using a conical horn antenna. The microwave radiation probes from the front side of the sample. The combination of a backside pump and frontside probe allows the horn antenna to be brought close to the sample for maximum collection of reflected signal. Using a circulator, the microwave radiation is launched and collected by a conical horn antenna. The collected radiation is sent to a microwave detector by a circulator. The sample is placed in a low-vibration cryostat and cooled to a temperature of 100 K. The setup diagram can be seen in Fig. 3.7.

When carriers are optically excited by the pump beam, $t = 0$, a hot distribution of electron-hole pairs throughout the T2SL absorber is generated, which perturbs the T2SL into a nonequilibrium state. These generated carriers then cool, or relax, to the band edges of the T2SL altering the conductivity. This change in conductivity is probed by microwave radiation. The conductivity decays for varying injected carrier densities are shown in Fig. 3.6. For large concentrations of injected carriers the initial

signal decays relatively fast, due to higher order recombination mechanisms such as Auger. Further in the decay, for example $t = 10000ns$, the decay rate resembles that of a single-exponential decay which relates to the characteristics of the minority carrier lifetime. For small concentrations of injected carriers the decay rate is single exponential, which looks linear on a log plot, due to the injected carrier density being dominated by low density recombination terms (i.e. minority carrier lifetime), in this case SRH. To properly resolve the influence of specific recombination terms, a calibration of the signal as a function of excess carrier density is performed.

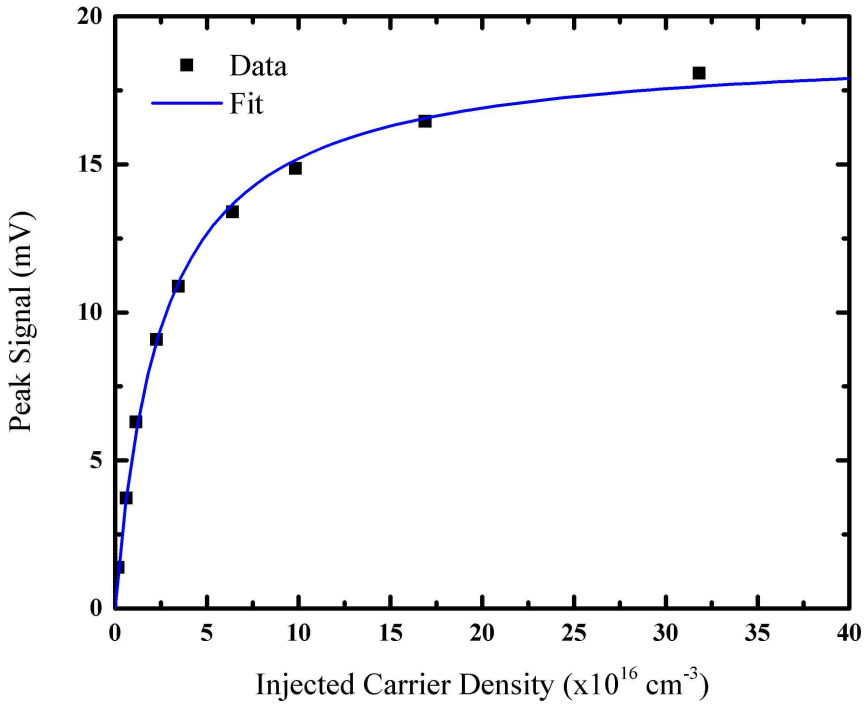

Figure 3.8: Peak reflected microwave signal as a function of injected carrier density, at 100K (black squares). The peak signal is taken shortly after zero time. The blue curve is a best for to the data.

Fig. 3.8 shows a calibration curve fit to the peak signal from reflected microwaves as a function of injected carrier densities, n_{inj}. This calibration curve is used to

determine the excess carrier density at a specific reflected microwave signal ($n_{inj} = \Delta n(t = 0)$). Using this calibration the temporal response of the excess carrier density can be found. Essentially, the signal can now be converted to $\Delta n(t)$ to permit more refined analysis. At large Δn the lifetime is short, whereas at small Δn the lifetime is considerably longer. This is due to the differing recombination terms. To resolve the carrier lifetime from these curves, the temporal response of the carrier density was converted to instantaneous lifetime using

$$\tau^{-1} = -\frac{1}{\Delta n}\frac{d\Delta n}{dt}. \tag{3.17}$$

The resulting instantaneous carrier lifetime with associated lifetime fit is shown in Fig. 3.9. The lifetime is fit using the carrier lifetime equation describing the recombination of a n-type semiconductor as discussed in Chapter 2,

$$\tau^{-1} = \frac{n_0 + \Delta n}{\tau_{h_0}(n_0 + \Delta n) + \tau_{e_0}(\Delta n)} + B(n_0 + \Delta n) + C_n(n_0 + \Delta n)^2. \tag{3.18}$$

By injecting a broad spectrum of carrier densities, multiple recombination characteristics can be found from fitting, such as SRH, radiative, Auger, and doping density. It is found that the SRH lifetimes are $3.51\mu s$ and $4.08\mu s$ for the hole and electron trapping lifetimes, respectively, the radiative recombination coefficient is found to be 4.58×10^{-11} cm^{3}s^{-1}, the Auger recombination coefficient is found to be 1.88×10^{-26} cm^{6}s^{-1}, and the doping is fit to be $4.39 \times 10^{14} cm^{-3}$.

Using a least squares regression approach for fitting of the instantaneous lifetime, the error in fit, or confidence bound, is found using the resulting covariance matrix. For the fit shown in Fig. 3.9, the 95% confidence interval for the SRH hole lifetime is

3.42 - 3.60 μs, 3.7 - 4.46 μs for the SRH electron lifetime, $4.21 - 4.56 \times 10^{-11}$ cm^{3}s^{-1} for the radiative recombination coefficient, $1.87 - 1.89 \times 10^{-26}$ cm^{6}s^{-1} for the Auger recombination coefficient, and $3.9 - 5.2 \times 10^{14} cm^{-3}$ for the electron doping level. The spread in confidence in the SRH hole lifetime is due to the spread in data at low excess carrier densities. The relatively small spread in confidence of the Auger coefficient is due to the low noise data at high excess carrier densities. The similar spread in confidence of the SRH electron lifetime, radiative coefficient, and doping level is due to all three parameters impacting the recombination rate at moderate excess carrier density levels. Simply put, small variations in these three parameters can statistically satisfy fitting of the instantaneous carrier lifetime which leads to a larger confidence bound.

3.4.2 Frequency modulated conductance

A common method of measuring carrier lifetime in silicon photovoltaics [7], [8], frequency modulated photoconductivity (FMP) is a very competitive method of measuring the lifetime at a specific carrier density. As was described in Frequency modulated photoluminescence, the carrier density is described as

$$\frac{d\Delta n}{dt} = G_{DC} + G_{AC}\cos(\omega t) - \Delta n[A + Bn + Cn^2]. \tag{3.19}$$

For the case of small modulation ($G_{DC} \gg G_{AC}$), Eq. 3.19 can be numerically solved, showing that these higher order recombination terms do not impact the carrier density response. However, for large modulation ($G_{DC} \propto G_{AC}$) these higher order recombination terms (the Auger and radiative recombination) do begin to impact

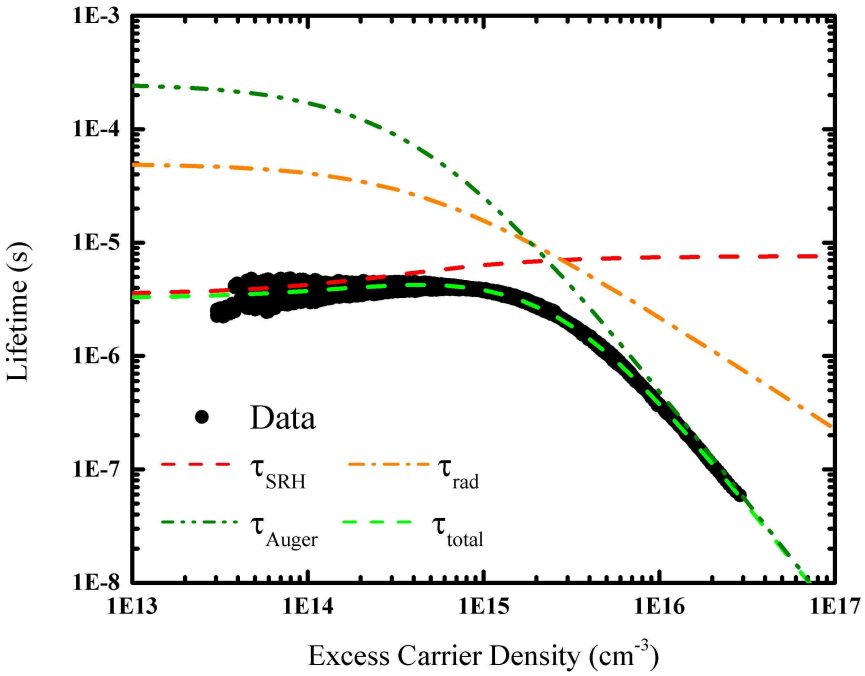

Figure 3.9: Carrier lifetime as a function of excess carrier densityfor a n-type doped MWIR InAs/InAsSb T2SL at a temperature of 100 K. The black circles correspond to the instantaneous carrier lifetime. The dashed red, dashed-dotted orange, and dashed-dot-dot green curve correspond to the SRH, radiative, and Auger lifetimes, respectively. The dashed bright green curve corresponds to the total lifetime.

the carrier density and can be seen in higher harmonic terms of the modulation frequency. This becomes a very interesting method to analyze the recombination mechanisms in an non-trivial way, which is the focus of Chapter 4.

In general, the method of choice is small modulation. For this method, the carrier density can be described as

$$\Delta n(t) = \tau G_{DC} + \frac{\tau G_{AC}}{\sqrt{1+\tau^2\omega^2}}\cos(\omega t - \phi), \tag{3.20}$$

where $\phi = \arctan(1/\tau\omega)$, which is analogous to FMPL. For more detail on the

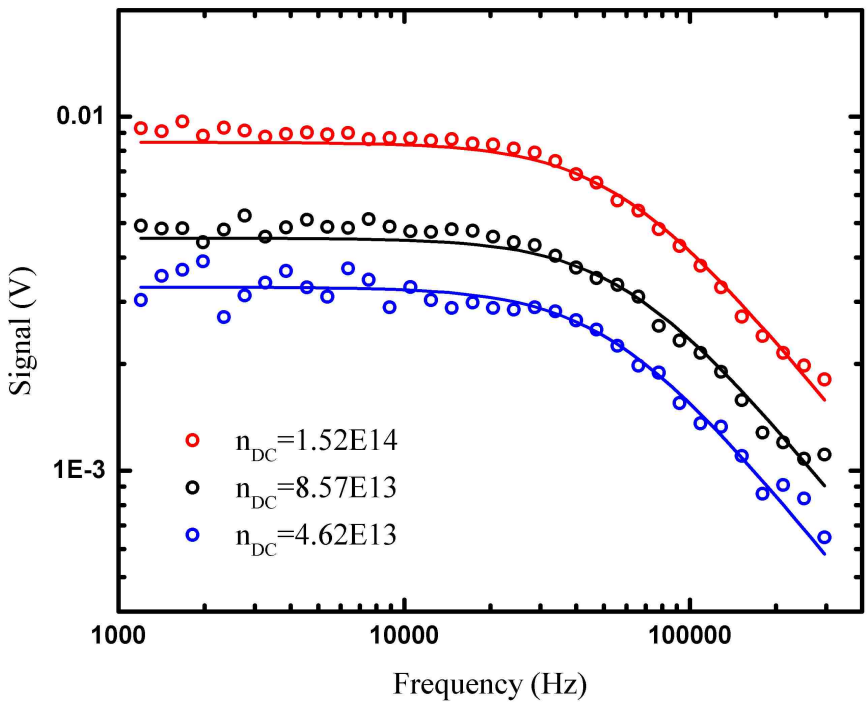

Figure 3.10: Frequency response data of the InAs/InAsSb T2SL sample for varying DC generation levels. The sample was cryogenically cooled to 100 K.

derivation of this equation, please refer to the Chap. 3.3.

Fig. 3.10 shows the frequency response of an InAs/InAsSb T2SL at a temperature of 100 K measured by frequency-modulated photoconductance. In this measurement, the pump was a 1625 nm laser with a $1/e$ spot size of 1.2 mm. The microwave apparatus is the same as in TMR, shown in Fig. 3.7. These frequency responses correspond to excess carrier densities that correlate to the minority carrier lifetime, $n_{DC} = 4.26\times10^{13}-1.52\times10^{14}$ cm^{-3}. At low frequency values the response is relatively flat. When the frequency is swept to greater than 20 kHz the modulation response begins to roll-off. The 3dB point of the three curves is found to be approximatley 80 kHz resulting in lifetime values of 3.31 μs, 3.28 μs, and 3.44 μs, from lowest carrier

density to highest.

3.5 References

[1] D. R. Rhiger, E. P. Smith, B. P. Kolasa, J. K. Kim, J. F. Klem, and S. D. Hawkins, "Analysis of iii–v superlattice nbn device characteristics," *Journal of Electronic Materials*, vol. 45, no. 9, pp. 4646–4653, 2016, ISSN: 1543-186X. DOI: 10.1007/s11664-016-4545-y. [Online]. Available: http://dx.doi.org/10.1007/s11664-016-4545-y.

[2] E. A. Kadlec, B. V. Olson, M. D. Goldflam, J. K. Kim, J. F. Klem, S. D. Hawkins, W. T. Coon, M. A. Cavaliere, A. Tauke-Pedretti, T. R. Fortune, C. T. Harris, and E. A. Shaner, "Effects of electron doping level on minority carrier lifetimes in n-type mid-wave infrared inas/inas1xsbx type-ii superlattices," *Applied Physics Letters*, vol. 109, no. 26, p. 261 105, 2016. DOI: 10.1063/1.4973352. eprint: http://dx.doi.org/10.1063/1.4973352. [Online]. Available: http://dx.doi.org/10.1063/1.4973352.

[3] R. K. Ahrenkiel, B. M. Keyes, and D. J. Dunlavy, "Intesity dependent minority carrier lifetime in iii-v semiconductors due to saturation of recombination centers," *J. Appl. Phys.*, vol. 70, p. 225, 1991.

[4] B. C. Connelly, G. D. Metcalfe, H. Shen, and M. Wraback, "Study of recombination mechanisms limiting the performance of Sb-based III-V type-II superlattices for infrared detectors," *Proc. of SPIE*, vol. 8155, p. 81550L, 2004.

[5] Y. Aytac, B. V. Olson, J. K. Kim, E. A. Shaner, S. D. Hawkins, J. F. Klem, M. E. Flatt, and T. F. Boggess, "Effects of layer thickness and alloy composition

on carrier lifetimes in mid-wave infrared inas/inassb superlattices," *Applied Physics Letters*, vol. 105, no. 2, 022107, 2014. DOI: http://dx.doi.org/10.1063/1.4890578. [Online]. Available: http://scitation.aip.org/content/aip/journal/apl/105/2/10.1063/1.4890578.

[6] B. V. Olson, L. M. Murray, J. P. Prineas, M. E. Flatté, J. T. Olesberg, and T. F. Boggess, "All-optical measurement of vertical charge carrier transport in mid-wave infrared InAs/GaSb type-II superlattices," *Appl. Phys. Lett.*, vol. 102, p. 202 101, 2013.

[7] R. Ahrenkiel and S. Johnston, "Lifetime analysis of silicon solar cells by microwave reflection," *Solar Energy Materials and Solar Cells*, vol. 92, no. 8, pp. 830 –835, 2008, ISSN: 0927-0248. DOI: http://dx.doi.org/10.1016/j.solmat.2008.01.022. [Online]. Available: http://www.sciencedirect.com/science/article/pii/S0927024808000330.

[8] R. Schieck and M. Kunst, "Frequency modulated microwave photoconductivity measurements for characterization of silicon wafers," *Solid-State Electronics*, vol. 41, no. 11, pp. 1755 –1760, 1997, ISSN: 0038-1101. DOI: http://dx.doi.org/10.1016/S0038-1101(97)00149-4. [Online]. Available: http://www.sciencedirect.com/science/article/pii/S0038110197001494.

Chapter 4

Measurement of recombination mechanisms using multiple harmonics

Type-II strained-layer superlattices (T2SL) are receiving increased interest as mid-wave infrared (MWIR) and long-wave infrared (LWIR) detector absorbers due to their potential Auger suppression[1], [2] and ability to be integrated into complex device structures.[3] Although HgCdTe based detection systems still excel in device performance, T2SLs are seeing comparable dark currents.[4], [5] The two T2SLs commonly reported for detector applications are InAs/Ga_{1-x} In_x Sb and InAs/In As_{1-x} Sb_x. Flatte *et al.*[6] proposed that longer minority carrier lifetimes in InAs/GaSb superlattices would lead to a surpassing of HgCdTe dark current performance. However, these lifetimes have yet to be achieved with some studies suggesting the existence of a native-defect associated with GaSb that limits the carrier lifetime.[7], [8] These

limitations have led to further research into Ga-free materials. One such material is InAs/InAs$_{1-x}$Sb$_x$, which has shown long minority carrier lifetimes, τ ~10 μs, rendering it promising for use as an infrared (IR) detector.[9], [10] As InAs/InAs$_{1-x}$Sb$_x$

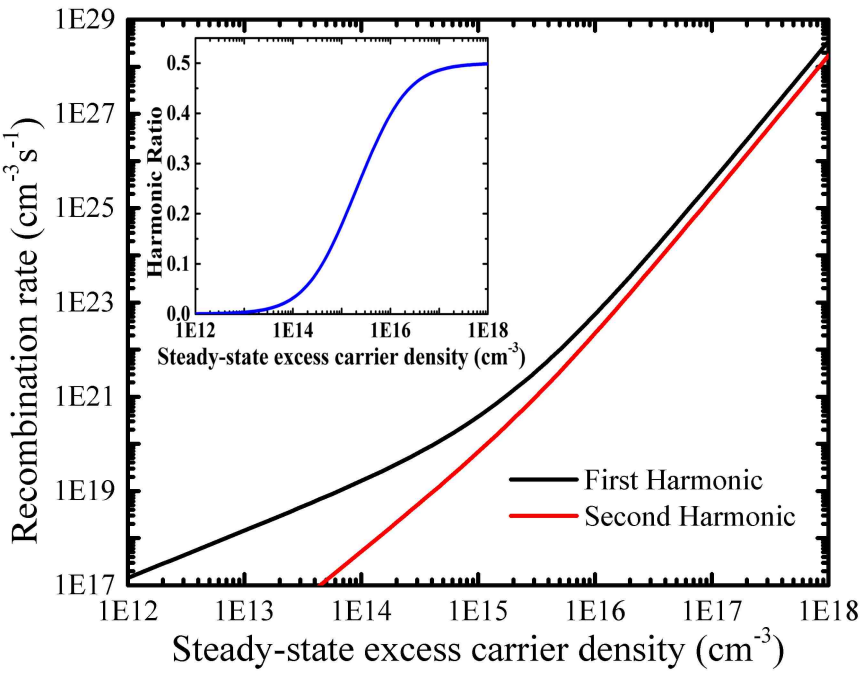

Figure 4.1: An instructive approach to analyzing the first and second harmonic of the recombination rate, Eq. 4.1c, where the excess carrier density is represented as Eq. 4.3 with $\gamma = 2$, $A^{-1} = 3.5\mu s$, $B = 2\times10^{-10} cm^3 s^{-1}$, and $C = 1.9\times10^{-26} cm^6 s^{-1}$. The inset shows the ratio of the second harmonic to the first as a function of steady-state excess carrier density.

T2SL growth has been further developed, the minority carrier lifetime has increased and background doping density has decreased.[11] This progression has created a challenge for standard pulsed excitation time-resolved photoluminescence (TRPL) measurements. In TRPL, the measured minority carrier lifetime is accurate at excited carrier levels below the majority carrier background doping level. At carrier densities above the background doping (high-injection), the lifetime is more chal-

lenging to obtain due to the dependence of carrier density on photoluminescence (PL) intensity. Another widely-used technique, known as frequency modulated photoluminescence (FMPL), uses DC carrier generation with small-signal modulation to measure carrier lifetime.[12]–[14] FMPL has the advantage of using a lock-in amplifier to improve the signal to noise ratio. However, this technique is still dependent on the capture of photoluminescence from the T2SL and requires relatively large incident fluence levels to reach large carrier densities in order to properly probe high-injection recombination. As the bandgap energy of the material under test is pushed to longer

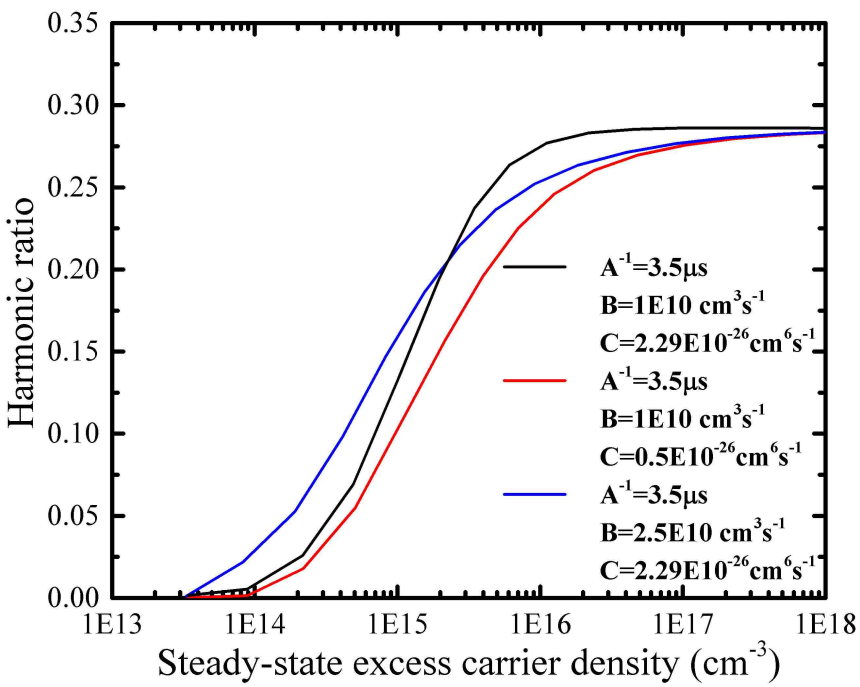

Figure 4.2: Numerical simulation results of Eq. 4.1a represented by the 2^{nd} harmonic divided by the 1^{st} harmonic. The curves shown were found by simulation the following values: $A^{-1} = 3.5\ \mu$s, $B = 1 \times 10^{-10}$ cm^{3}s^{-1}, $C = 2.29 \times 10^{-26}$ cm^{6}s^{-1}, black line, $A^{-1} = 3.5\ \mu$s, $B = 1 \times 10^{-10}$ cm^{3}s^{-1}, $C = 0.5 \times 10^{-26}$ cm^{6}s^{-1}, red line, and $A^{-1} = 3.5\ \mu$s, $B = 2.5 \times 10^{-10}$ cm^{3}s^{-1}, $C = 2.29 \times 10^{-26}$ cm^{6}s^{-1}, blue line.

IR wavelengths, the detectivity of associated detectors used for capturing the emitted PL decreases, thus, limiting the capabilities of PL based lifetime measurements. A more sensitive technique is to measure changes in conductivity induced by excited electron-hole pairs by monitoring changes in reflection of microwave radiation. Measurement techniques based on microwave probes of photoconductivity have been shown on an assortment of different materials[15], [16], including T2SL materials in the very long-wave infrared[17], LWIR[18], and MWIR[19] regions. Here, we will use microwave radiation to investigate two recombination regimes: a steady-state carrier generation with small-signal modulation, known as frequency modulated photoconductivity (FMP), and a large-modulation generation (LMG) where the pump modulation amplitude is on the order of the steady-state pump generation. We analyze second harmonic terms of the excitation frequency in LMG to extract information on radiative and Auger recombination, as the higher order harmonic terms are solely dependent on the high-injection recombination. These measurement techniques are then compared to results obtained from time-resolved microwave reflectance (TMR).

4.1 Simulations

The differential equation describing time dependent carrier density is defined by Eq. 4.1a where the carrier generation, G, is described by Eq. 4.1b, the recombination rate, R, is described as Eq. 4.1c, γ is the ratio of DC generation to AC modulation ($\gamma = G_{DC}/G_{AC}$), ω is the angular frequency, t is time, A is the Shockley-Read-Hall (SRH) recombination rate, B is the radiative recombination coefficient, and C is the

Auger recombination coefficient

$$\frac{d\Delta n}{dt} = G - R, \tag{4.1a}$$

$$G(t) = G_0(1 + \frac{\cos(\omega t)}{\gamma}), \tag{4.1b}$$

$$R(n) = \Delta n(A + Bn + Cn^2). \tag{4.1c}$$

The carrier density is described as $n = n_0 + \Delta n$, where n_0 is the doping density and Δn is the excess carrier density. Generally, the generation term is written as $G = G_0 + G_1 \cos(\omega t)$, where G_0 is the static generation constant and G_1 is the modulation generation constant. Here, we have chosen to incorporate γ in the generation term as the DC to AC ratio will play a pivotal role in the signal level of the generated second harmonic. Assuming the excess carrier density is in a region dominated by SRH recombination, the carrier lifetime, τ, will be approximately equal to A^{-1}. For this special case Eq. 4.1a may be analytically solved giving

$$\Delta n(t) = G_0\tau + \frac{G_0}{\gamma\sqrt{1 + (\omega\tau)^2}} \cos(\omega t - \phi), \tag{4.2}$$

where $\phi(\omega) = \arctan((\tau\omega)^{-1})$. As the modulation frequency is swept, the AC signal will have a roll-off proportional to $\Delta n_{AC}(\omega) \propto \frac{G_0}{\gamma\sqrt{1+(\omega\tau)^2}}$. From the AC roll-off, the carrier lifetime of the material under test can be found. For low frequencies ($\omega \ll \frac{\sqrt{3}}{\tau}$) and small-signal modulation ($\gamma \gg 1$) the excess carrier density can be described as

$$\Delta n(t, \omega) = n_{DC} + \frac{n_{DC}}{\gamma} \cos(\omega t), \tag{4.3}$$

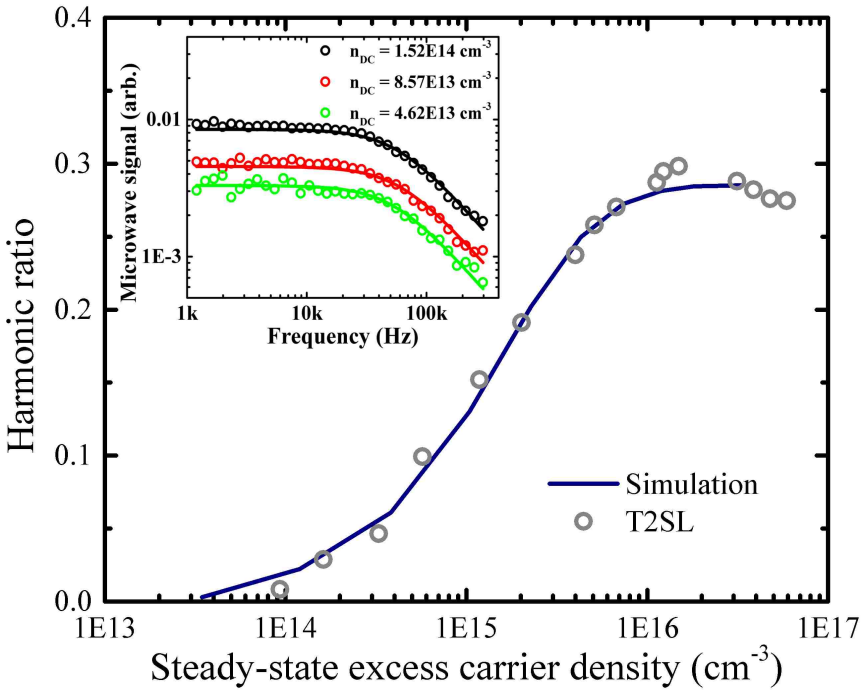

Figure 4.3: Measured ratio of $2^{nd}/1^{st}$ harmonic, grey circles. The blue line plot is a fit to the measured data via shooting-method from simulation results. Values obtained from the fit are $A^{-1} = 3.47$ μs ± 100 ns, $B = 1 \times 10^{-10}$ cm^{3}s^{-1}, $C = 2.29 \times 10^{-26}$ cm^{6}s^{-1}. The inset shows the frequency roll-off of microwave signal for three different static carrier densities that reside in the Shockley-Read-Hall limited lifetime region. The carrier lifetime found from these measurements was 3.47 ± 0.1 μs.

where n_{DC} is the steady-state excess carrier density, $n_{DC} = G_0\tau$. For instructive purposes, inserting Eq. 4.3 into Eq. 4.1c it can be shown that multiple harmonics directly relating to radiative and Auger recombination are present in this simplified picture of the recombination term. By separating the higher order cosine terms, it is also apparent that the second harmonic will be related to the first harmonic by a factor of $\frac{1}{\gamma}$ and the carrier density, as shown in Fig. 5.1. Taking the ratio of the second harmonic divided by the first harmonic at various carrier density levels, it

can be seen that the quotient asymptotically approaches a value that is dependent on B and C to a constant dependent on γ, inset of Fig. 5.1. However, for situations where this restriction condition is not met, (i.e. recombination is not dominated by SRH processes) Eq. 4.1a cannot be easily solved. Therefore, determination of the influence of the radiative and Auger recombination must be performed numerically. Numerical simulations were performed to validate using the second harmonic with relation to the first harmonic as a means of measuring the recombination coefficients, A, B, and C. Eq. 4.1a was numerically solved to obtain the carrier density dynamics using various generation values (as given by Eq. 4.1b) and recombination mechanisms (as given by Eq. 4.1c). The simulation was performed in two regimes. First, large γ values were examined ($\gamma \gg 1$) to numerically solve for steady-state carrier density as a function of the static generation level, standard FMP. The simulation sweeps the generation modulation frequency and measures the AC roll-off of the numerical solution. From the 3dB point of the AC roll-off, the carrier lifetime at a specific static generation value can be calculated. From the carrier lifetime and generation value, the steady-state carrier density can be analytically solved and compared to the simulated temporal response acquired from the numerical solution. These steady-state carrier densities, in relation to the static carrier generation term (G_0), are used as the steady-state carrier density for the LMG simulation. This is done because the LMG sweeps through relatively large carrier densities, yet the center point will be the referenced carrier density. Second, large modulation ($\gamma \approx 1$) at a single frequency below AC roll-off ($\omega \ll \frac{\sqrt{3}}{\tau}$) was investigated at various steady-state carrier densities. The simulated temporal solution is analyzed using lock-in amplifier theory to calculate the first and second harmonics. The results are then compared as a function of steady-state carrier density. Fig.5.2 shows results of sim-

ulation of various recombination coefficient parameters. Distinct differences exist in the slope of the harmonic ratio vs. carrier density, demonstrating the viability of this technique for proper characterization of the recombination mechanisms of T2SL and other materials with similar recombination properties.

4.2 Sample and methods

To verify the performance of both the FMP and LMG approaches, measurement of recombination mechanisms of an InAs/$InAs_{1-x}Sb_x$ T2SL were performed. The sample was grown by molecular beam epitaxy (MBE) on an n-doped GaSb substrate. The structure consisted of a 100 nm AlAsSb cladding, the T2SL layer, 100 nm AlAsSb cladding, and capped with 70 nm of InAsSb. The AlAsSb cladding layers confine the photo-generated carriers in the absorber region to help prevent unwanted recombination processes in the substrate and surface. The T2SL absorber layer consists of 750 periods of slightly doped 4.07 nm InAs and 1.29 nm $InAs_{1-x}Sb_x$. The bandgap energy of the T2SL was measured from PL taken at 80 K and found to be 246 meV. A low-vibration cryostat was used to cool the sample to 100 K. Carriers were generated in the absorber region using a 1625 nm electrically modulated laser. The modulation of the pump beam was referenced using an InGaAs photodiode. The incident pump power was controlled using two nanoparticle linear film polarizers in series. The first polarizer was used to attenuate power and the second polarizer was held constant to ensure a consistent Fresnel reflection for all incident powers. The microwave radiation was sourced using a 95-GHz Gunn diode and was launched and collected using a conical horn antenna. The reflected microwave signal was directed

to a detector using a circulator and analyzed using a Zurich HF2LI Lock-in amplifier.

4.3 Results

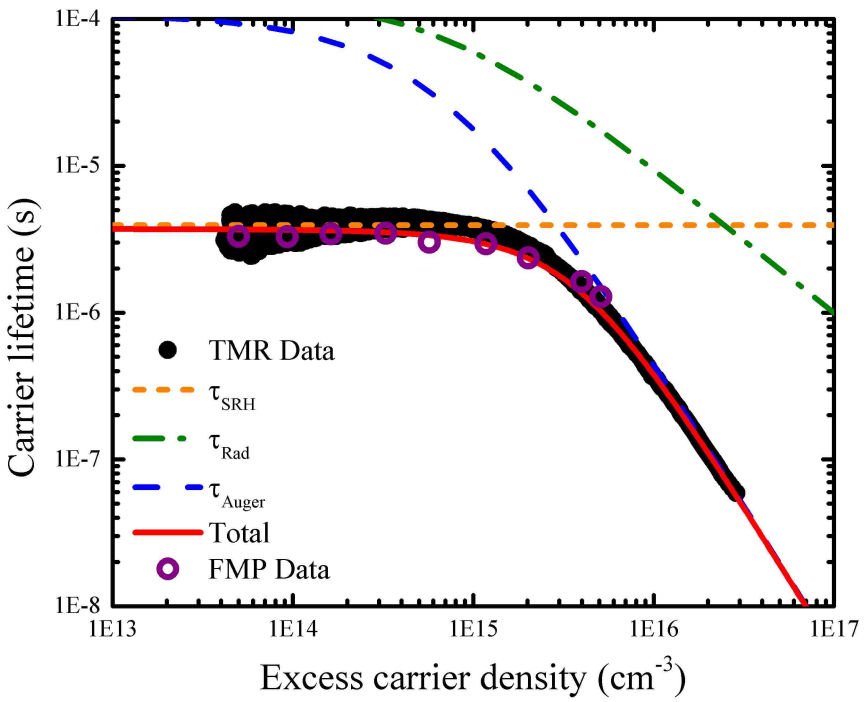

Figure 4.4: Carrier lifetime as a function of excess carrier density for a n-type doped mid-wave infrared InAs/$InAs_{1-x}Sb_x$ type-II superlattice at a temperature of 100 K. The black curve corresponds to the instantaneous carrier lifetime found from time-resolved microwave reflectance measurements. The dashed, short-dashed, and dash-dotted curves correspond to the individual lifetimes of the various carrier recombination mechanisms found from fitting of the instantaneous carrier lifetime. The purple circles correspond to single-point carrier lifetime values measured using frequency modulated photoconductivity.

To calculate the steady-state carrier density for a particular incident laser fluence (G_0), the carrier lifetime was measured for a range of steady-state injected carrier

densities by means of FMP, inset of Fig. 4.3. Aligning with the procedure done in simulation, the carrier density associated with the incident laser fluence is used as a steady-state carrier density calibration in the large modulation measurement. The harmonics were measured using LMG at $f = 1.2$ kHz. Fig. 4.3 shows the resulting ratio of the second harmonic to the first harmonic at steady-state carrier densities calculated from the FMP. A shooting-method fit, found from simulating various recombination mechanisms, to the collected data provides the recombination coefficients, $A^{-1} = 3.47$ μs ± 100 ns, $B = 1 \times 10^{-10}$ cm^{3}s^{-1} and $C = 2.29 \times 10^{-26}$ cm^{6}s^{-1}. The measured recombination coefficients using the LMG approach are in close agreement with TMR measurements performed on the sample under test.

The TMR measurement utilizes a 5 ns pulsed 3.7 μm laser to optically inject carriers into the T2SL layer. The resulting carrier recombination is probed using continuous-wave 95-GHz radiation reflected from the sample. TMR data were collected and analyzed as described by Ref. [18]–[21]. The instantaneous lifetime data were fit using an equation that takes into account SRH, radiative, and Auger recombination as[19]

$$\tau^{-1} = A + B(n_0 + \Delta n) + C(n_0 + \Delta n)^2. \tag{4.4}$$

The carrier lifetime as a function of excess carrier density and fit to data is shown in Fig. 4.4. Fitting of the instantaneous carrier lifetime provides recombination coefficients of $A^{-1} = 3.72$ μs, $B = 1.5 \times 10^{-11}$ cm^{3}s^{-1}, and $C = 1.95 \times 10^{-26}$ cm^{6}s^{-1} and a doping density of $n_0 = 2.59 \times 10^{15}$ cm^{-3}. For comparison, the lifetimes measured by frequency modulated carrier generation for specific steady-state carrier densities, which are included in the LMG calibration, are included in Fig. 4.4. These single-point lifetime measurements match well with the TMR data showing viability

of both the FMP and LMG approaches.

4.4 Conclusion

Frequency modulated photoconductivity, both small-signal (FMP) and large modulation (LMG), probed by microwave reflectance was used to measure recombination mechanisms in an InAs/$InAs_{1-x}Sb_x$ T2SL by measuring the second harmonic induced from single-frequency modulated carrier generation. It was shown through simulation and measurement that the ratio of the second to the first harmonic of generated carrier density provides a viable means of measuring the recombination mechanisms due to the characteristic of it being solely dependent on the high-injection recombination mechanisms. The results found from modulated photoconductivity agree with the commonly used time-resolved microwave reflectance approach. Significant advantages of this technique are the ability to probe at lower carrier densities to fit Auger recombination, the requirement of basic telecom lasers, and the use of phase sensitive detection to increase signal-to-noise of the system.

4.5 References

[1] C. H. Grein, P. M. Young, and H. Ehrenreich, "Minority carrier lifetimes in ideal InGaSb/InAs superlattices," *Appl. Phys. Lett.*, vol. 61, pp. 2905–2907, 1992.

[2] C. H. Grein, P. M. Young, M. E. Flatté, and H. Ehrenreich, "Long wavelength InAs/InGaSb infrared detectors: Optimization of carrier lifetimes," *J. Appl. Phys.*, vol. 78, pp. 7143–7152, 1995.

[3] S. Maimon and G. W. Wicks, "Nbn detector, an infrared detector with reduced dark current and higher operating temperature," *Appl. Phys. Lett.*, vol. 89, p. 151 109, 2006.

[4] D. R. Rhiger, "Performance comparison of long-wavelength infrared type-ii superlattice devices with HgCdTe," *J. Electron. Mat.*, vol. 40, pp. 1815–1822, 2011.

[5] D. R. Rhiger, E. P. Smith, B. P. Kolasa, J. K. Kim, J. F. Klem, and S. D. Hawkins, "Analysis of iii–v superlattice nbn device characteristics," *Journal of Electronic Materials*, vol. 45, no. 9, pp. 4646–4653, 2016, ISSN: 1543-186X. DOI: 10.1007/s11664-016-4545-y. [Online]. Available: http://dx.doi.org/10.1007/s11664-016-4545-y.

[6] M. E. Flatté and C. H. Grein, "Theory and modeling of type-II strained-layer superlattice detectors," *Proc. of SPIE*, vol. 7222, 72220Q, 2009.

[7] D. Donetsky, G. Belenky, S. Svensson, and S. Suchalkin, "Minority carrier lifetime in type-2 InAs-GaSb strained-layer superlattices and bulk HgCdTe materials," *Appl. Phys. Lett.*, vol. 97, p. 052 108, 2010.

[8] S. P. Svensson, D. Donetsky, D. Wang, H. Hier, F. J. Crowne, and G. Belenky, "Growth of type II strained layer superlattice, bulk InAs and GaSb materials for minority lifetime characterization," *J. Crystal Growth*, vol. 334, pp. 103–107, 2011.

[9] E. H. Steenbergen, B. C. Connelly, G. D. Metcalfe, H. Shen, M. Wraback, D. Lubyshev, Y. Qiu, J. M. Fastenau, A. W. K. Liu, S. Elhamri, O. O. Cellek, and Y.-H. Zhang, "Significantly improved minority carrier lifetime observed in a long-wavelength infrared III-V type-II superlattice comprised of InAs/InAsSb," *Appl. Phys. Lett.*, vol. 99, p. 251 110, 2011.

[10] B. V. Olson, E. A. Shaner, J. K. Kim, J. F. Klem, S. D. Hawkins, L. M. Murray, J. P. Prineas, M. E. Flatté, and T. F. Boggess, "Time-resolved optical measurements of minority carrier recombination in a mid-wave infrared InAsSb alloy and InAs/InAsSb superlattice," *Appl. Phys. Lett.*, vol. 101, p. 092 109, 2012.

[11] E. A. Kadlec, B. V. Olson, M. D. Goldflam, J. K. Kim, J. F. Klem, S. D. Hawkins, W. T. Coon, M. A. Cavaliere, A. Tauke-Pedretti, T. R. Fortune, C. T. Harris, and E. A. Shaner, "Effects of electron doping level on minority carrier lifetimes in n-type mid-wave infrared inas/inas1xsbx type-ii superlattices," *Applied Physics Letters*, vol. 109, no. 26, p. 261 105, 2016. DOI: 10.1063/1.4973352. eprint: http://dx.doi.org/10.1063/1.4973352. [Online]. Available: http://dx.doi.org/10.1063/1.4973352.

[12] D. Donetsky, S. Anikeev, N. Gu, G. Belenky, S. Luryi, C. A. Wang, D. A. Shiau, M. Dashiell, J. Beausang, and G. Nichols, "Analysis of recombination processes in 0.5-0.6 ev epitaxial GaInAsSb lattice-matched to GaSb," *Proc. of SPIE*, 2004.

[13] J. E. Martin and L. E. Shea-Rohwer, "Lifetime determination of materials that exhibit a stretched exponential luminescent decay," *Journal of Luminescence*, vol. 121, 2006. DOI: doi:10.1016/j.jlumin.2005.12.043.

[Online]. Available: http://ac.els-cdn.com/S0022231305003601/1-s2.0-S0022231305003601-main.pdf?_tid=afadf62a-2550-11e7-913d-00000aacb35e&acdnat=1492641593_7ba712166cab1f3d741c0ca67ebdf94f.

[14] D. Donetsky, S. P. Svensson, L. E. Vorobjev, and G. Belenky, "Carrier lifetime measurements in short-period InAs/GaSb strained-layer superlattice structures," *Appl. Phys. Lett.*, vol. 95, p. 212 104, 2009.

[15] R. Ahrenkiel and S. Johnston, "Lifetime analysis of silicon solar cells by microwave reflection," *Solar Energy Materials and Solar Cells*, vol. 92, no. 8, pp. 830 –835, 2008, ISSN: 0927-0248. DOI: http://dx.doi.org/10.1016/j.solmat.2008.01.022. [Online]. Available: http://www.sciencedirect.com/science/article/pii/S0927024808000330.

[16] R. Schieck and M. Kunst, "Frequency modulated microwave photoconductivity measurements for characterization of silicon wafers," *Solid-State Electronics*, vol. 41, no. 11, pp. 1755 –1760, 1997, ISSN: 0038-1101. DOI: http://dx.doi.org/10.1016/S0038-1101(97)00149-4. [Online]. Available: http://www.sciencedirect.com/science/article/pii/S0038110197001494.

[17] H. J. Haugan, G. J. Brown, B. V. Olson, E. A. Kadlec, J. K. Kim, and E. A. Shaner, "Demonstration of long minority carrier lifetimes in very narrow bandgap ternary inas/gainsb superlattices," *Applied Physics Letters*, vol. 107, no. 13, 131102, 2015. DOI: http://dx.doi.org/10.1063/1.4932056. [Online]. Available: http://scitation.aip.org/content/aip/journal/apl/107/13/10.1063/1.4932056.

[18] B. V. Olson, C. H. Grein, J. K. Kim, E. A. Kadlec, J. F. Klem, S. D. Hawkins, and E. A. Shaner, "Auger recombination in long-wave infrared inas/inassb

type-ii superlattices," *Appl. Phys. Lett.*, vol. 107, no. 26, 261104, 2015. DOI: http://dx.doi.org/10.1063/1.4939147. [Online]. Available: http://scitation.aip.org/content/aip/journal/apl/107/26/10.1063/1.4939147.

[19] B. V. Olson, E. A. Kadlec, J. K. Kim, J. F. Klem, S. D. Hawkins, E. A. Shaner, and M. E. Flatté, "Intensity- and temperature-dependent carrier recombination in InAs/Inas1 − $x$sb$x$ type-ii superlattices," *Phys. Rev. Applied*, vol. 3, p. 044 010, 4 2015. DOI: 10.1103/PhysRevApplied.3.044010. [Online]. Available: http://link.aps.org/doi/10.1103/PhysRevApplied.3.044010.

[20] B. V. Olson, J. K. Kim, E. A. Kadlec, J. F. Klem, S. D. Hawkins, D. Leonhardt, W. T. Coon, T. R. Fortune, M. A. Cavaliere, A. Tauke-Pedretti, and E. A. Shaner, "Minority carrier lifetime and dark current measurements in mid-wavelength infrared InAs0.91Sb0.09 alloy nbn photodetectors," *Appl. Phys. Lett.*, vol. 107, no. 18, 183504, 2015. DOI: http://dx.doi.org/10.1063/1.4935159. [Online]. Available: http://scitation.aip.org/content/aip/journal/apl/107/18/10.1063/1.4935159.

[21] B. V. Olson, E. A. Kadlec, J. K. Kim, J. F. Klem, S. D. Hawkins, A. Tauke-Pedretti, W. T. Coon, T. R. Fortune, and E. A. Shaner, "Contactless measurement of equilibrium electron concentrations in n-type inas/inas1xsbx type-ii superlattices," *Applied Physics Letters*, vol. 109, no. 2, 022105, 2016. DOI: http://dx.doi.org/10.1063/1.4956351. [Online]. Available: http://scitation.aip.org/content/aip/journal/apl/109/2/10.1063/1.4956351.

Chapter 5

Effects of electron doping on InAs/InAsSb carrier lifetime

The following chapter was originally published as: E.A. Kadlec *et. al*,Effects of electron doping level on minority carrier lifetimes in n-type mid-wave infrared InAs/In As_{1-x} Sb_x type-II superlattices, *Appl. Phys. Lett.*, vol. 109, no. 26, 261105, (2016)

5.1 Introduction

The minority-carrier lifetime (τ_{MC}) and the electron doping density (n_0) are crucial parameters that determine the performance of infrared (IR) photodetectors.[1], [2] For a diffusion current-dominated photodetector the dark current is inversely proportional to the product $n_0\tau_{MC}$, and described as[3]

$$J_{diff} = q\frac{n_i^2 W}{n_0\tau_{MC}}, \tag{5.1}$$

where n_i is the intrinsic carrier density, q is the electron charge, and W is either the absorber thickness or hole diffusion length, whichever is shorter. It can be seen from Eq. 5.1 that high doping levels and long minority carrier lifetimes would minimize diffusion current. However, since τ_{MC} is dependent on multiple carrier recombination mechanisms, all of which scale differently with n_0, there is a value of n_0 that minimizes dark diffusion current.

As HgCdTe (MCT) photodetector performance has shown limited progress in recent years,[4] new materials become imperative for the continual growth of IR detection. Through recent advancements, type-II superlattices (T2SLs) have shown potential for use as photodetectors. Auger suppression in InAs/$Ga_{1-x}In_xSb$ superlattices has been theorized and shown experimentally to be significant enough to surpass the dark current performance of MCT.[5]–[7] However, this material system has been limited by parasitic Shockley-Read-Hall (SRH) defects resulting in short minority carrier lifetimes.[8]–[10] Due to the limitations of this native parasitic defect, other T2SL materials have been investigated, such as InAs/$InAs_{1-x}Sb_x$. Long τ_{MC} values have been achieved in InAs/$InAs_{1-x}Sb_x$ T2SL structures[11]–[13] showing potential for use in IR detectors. A previous study by Höglund *et al.*[14] has presented the $n_0\tau_{MC}$ product over the doping range of 1.2×10^{15} cm^{-3} - 4.5×10^{15} cm^{-3} in InAs/$InAs_{1-x}Sb_x$ T2SLs. However, a systematic study over a much larger doping range is still lacking. The study presented in this *Letter* investigates carrier lifetimes in mid-wave infrared (MWIR) InAs/$InAs_{1-x}Sb_x$ T2SLs over the doping range 2×10^{14} cm^{-3} - 2×10^{16} cm^{-3} to determine the optimum $n_0\tau_{MC}$ product. Dark current in two InAs/$InAs_{1-x}Sb_x$ photodetectors of different doping (2×10^{14} cm^{-3} and 7.5×10^{15} cm^{-3}) are shown, demonstrating a reduction in dark current by

optimizing the doping level.

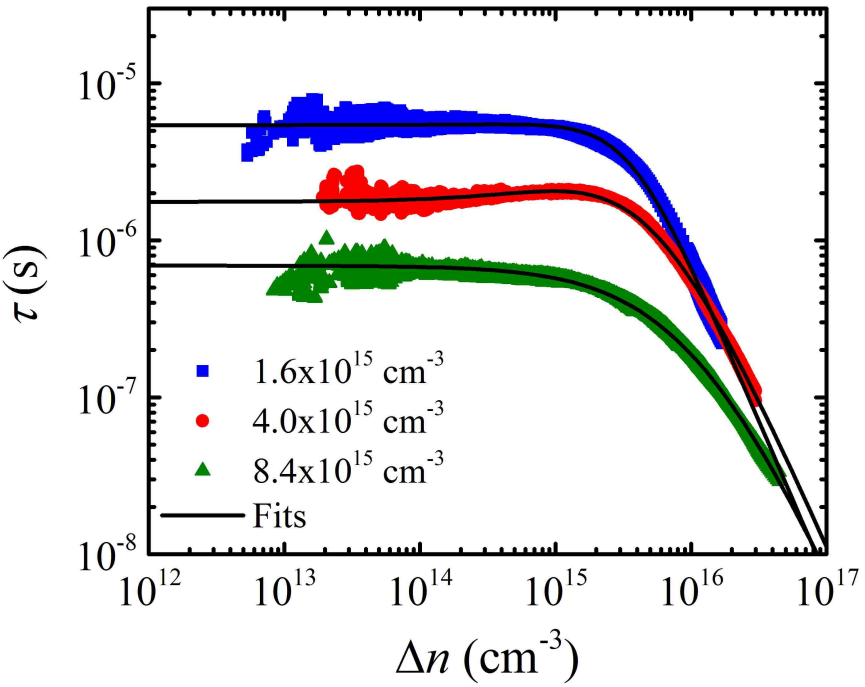

Figure 5.1: Instantaneous carrier lifetime as a function of excess carrier density for three n-type mid-wave infrared $InAs/InAs_{1-x}Sb_x$ type-II superlattice samples at a temperature of 125 K. The equilibrium electron concentrations (i.e. the net doping level) and carrier lifetimes are determined from fits to the lifetime data (black curves).

5.2 Sample and Method

We first conduct a survey of not intentionally doped (*nid*) and intentionally doped MWIR $InAs/InAs_{1-x}Sb_x$ T2SL material grown at Sandia National Laboratories with 100 K bandgap energies between 215 meV (5.76 μm) and 250 meV (4.96 μm). From this list, samples are screened based on both τ_{MC} and n_0. The samples with the longest lifetimes at a particular doping level have been kept, as these present current

limiting performance, resulting in the fourteen samples reported here. All samples are grown using molecular beam epitaxy on slightly n-type GaSb substrates. Absorber regions are approximately 4 μm thick. Appropriate cladding layers are present in all structures to ensure the measured minority carrier lifetimes are reflective of the narrow-bandgap T2SL region and not of carrier leakage into the substrate or surface recombination. In order to achieve doping above *nid* levels, either Si or Te are used as intentional n-type dopants. No significant effect on the resulting minority carrier lifetime is observed between the use of the two different dopants, and we do not differentiate between samples with Si or Te doping in this *Letter*. Compositions for the $InAs_{1-x}Sb_x$ alloy layer of the T2SL structure range from approximately 30% to 50% Sb.

Minority carrier lifetimes and doping levels are measured using the time-resolved microwave reflectance (TMR) apparatus described by Olson *et al.*[2] This apparatus utilizes a 5 ns pulsed IR laser to optically inject charge carriers into the T2SL absorbing layer of the sample under test. For these measurements substrate side illumination at the wavelength of 3.7 μm with a e^{-1} radius of 2.7 mm was used. The resulting carrier recombination decay is probed by 95 GHz continuous-wave microwave radiation reflected from the sample. The instantaneously excited carrier density is directly related to the reflected microwave power at a particular time through the change in sample conductivity that arises when the T2SL is perturbed from equilibrium. TMR data are collected and analyzed in the manner described previously by Ref. [2], [15], [16], resulting in carrier lifetimes as a function of excited carrier density (Δn).

Representative lifetime data from three T2SL samples of different doping levels

are shown in Fig. 5.1. All data presented are taken at 125 K and fit using an equation that takes into account SRH, radiative, and Auger recombination as[2]

$$\tau^{-1} = \tau_{SRH}^{-1} + \frac{B_r}{\phi}(n_0 + \Delta n) + C_n(n_0 + \Delta n)^2, \tag{5.2}$$

where τ_{SRH} is the SRH lifetime, B_r is the intrinsic radiative recombination coefficient, ϕ is the photon recycling factor, and C_n is the electron Auger recombination coefficient. It is assumed that the Auger-1 recombination process dominates over the Auger-7 process.[2], [15] For n-type doping, the SRH lifetime dependence on Δn and n_0 is

$$\tau_{SRH}^{-1} = \frac{n_0 + \Delta n}{\tau_{p_0}(n_0 + \Delta n) + \tau_{n_0}\Delta n}, \tag{5.3}$$

where τ_{p_0} and τ_{n_0} are the characteristic hole and electron SRH lifetimes.[17] Note, the doping level is explicitly taken into account in the fitting of the carrier lifetime data. Using Eqs. 5.2 and 5.3 to fit the measured carrier lifetime data allows for accurate determination of τ_{SRH}, the ratio B_r/ϕ, C_n, and n_0. The minority carrier lifetime is found using Eq. 5.2 with $\Delta n \ll n_0$.

More conventional carrier density measurement methods do exist, such as capacitance voltage (C-V) and Hall measurements.[18] However, these require device fabrication steps in order to make electrical contact to the material. C-V measurements in particular can also be highly dependent on the device architecture and geometry, and can be effected by parasitic capacitances. Extracting carrier concentrations from C-V data relies on accurate knowledge of the material's dielectric constant, which is not well known for T2SLs. [2], [16] Here, since we measure carrier lifetimes with very high fidelity at excited carrier densities both greater than and

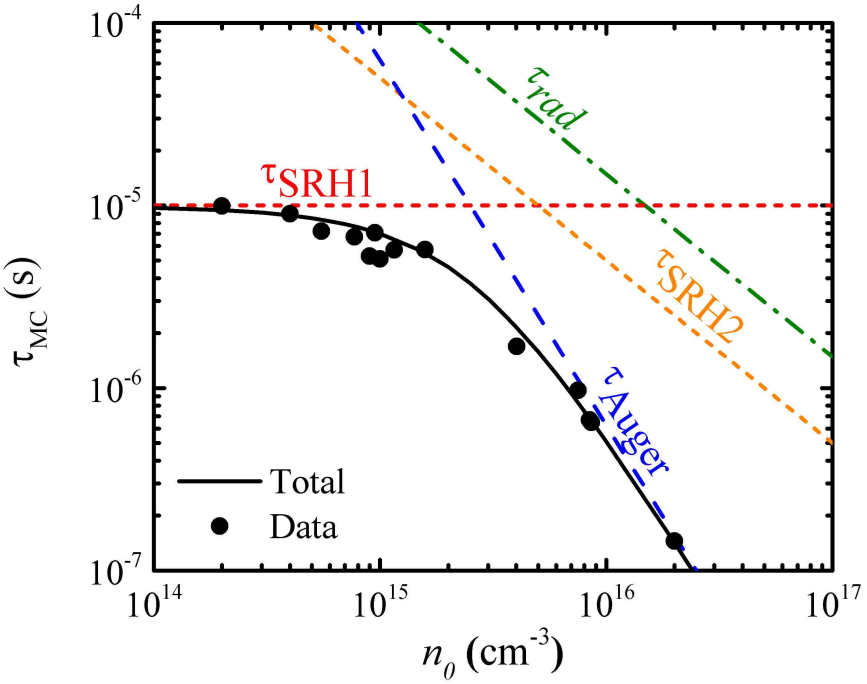

Figure 5.2: Measured minority carrier lifetimes as a function of doping density at a temperature of 125 K. The solid black curve is the best fit to data where $\tau_{MC}^{-1} = \tau_{SRH_1}^{-1} + \tau_{SRH_2}^{-1} + \tau_{rad}^{-1} + \tau_{Auger}^{-1}$. The dashed, short-dashed, and dashed-dotted curves correspond to the individual lifetimes of the various carrier recombination mechanisms that have been identified to contribute to the total minority carrier lifetime. τ_{SRH_1} is identified as the SRH lifetime associated with a native defect present in the T2SL material system and τ_{SRH_2} is an SRH lifetime that scales with the intentional doping level.

much less than the net doping level, accurate extraction of the doping level can be made from fitting carrier lifetime data. Uncertainty in the extracted doping level using this technique is dependent on the calibration of the initial optically injected carrier densities, which rely on accurate measurements of the pump energy and spot size, the superlattice absorption coefficient, and the assumption that every photon absorbed by the T2SL creates an electron-hole pair. This technique also requires the Auger recombination rate to be within a range where doping density has enough

influence to be measurable. For example, if the Auger rate is too small then the doping level will have little significance on the carrier lifetime leading to difficulty in extraction. The absorption coefficients in this work are calculated using 14-band **k·p** software (*SLKdp*, QuantCAD LLC). The estimated error in doping levels extracted from these high-fidelity lifetime data is approximately a factor of 2, which is similar to expected errors from such methods as C-V analysis. TMR also has the benefit of being completely non-contact and non-destructive, and does not require additional fabrication. For the three T2SL samples presented in Fig. 5.1, the extracted doping levels from lifetime fitting are 1.6×10^{15} cm^{-3}, 4.0×10^{15} cm^{-3}, and 8.4×10^{15} cm^{-3} with corresponding minority carrier lifetimes of 5.73 μs, 1.69 μs, and 0.68 μs, respectively.

5.3 Results

Repeating the described fitting procedure for the fourteen different T2SL samples in this study, a relationship between minority carrier lifetime and doping density is found, shown in Fig. 5.2 where the uncertainty in the minority carrier lifetime measurement is represented by the symbol size. In order to quantitatively investigate the dependence that τ_{MC} has with n_0, these data are analyzed using carrier recombination theory involving SRH, radiative, and Auger recombination. The minority carrier lifetime can be written as[19]

$$\tau_{MC}^{-1} = \sum_i \tau_{SRH_i}^{-1} + \tau_{rad}^{-1} + \tau_{Auger}^{-1}, \tag{5.4}$$

where τ_{SRH_i} is the SRH lifetime for the i-th defect level, τ_{rad} is the radiative lifetime, and τ_{Auger} is the Auger lifetime. Typically, when considering *nid* material, it is realistic to assume a single SRH defect level,[2] however this may not necessarily be the case for intentionally doped T2SLs. Previous work by Olson *et al.*[19] assumed a unique SRH defect level associated with the intentional dopant and found this SRH level to be approximately 70±10 meV into the T2SL bandgap, compared to 130±20 meV for the native SRH defect center. Thus, we assume that there are two unique SRH defect levels with associated SRH lifetimes for this analysis; one from the native defect that is independent of the doping level (τ_{SRH_1}) and a second created by the intentional dopant atoms (τ_{SRH_2}) that is dependent on the doping level.

The SRH lifetime is a complicated function of characteristic lifetimes and various carrier densities. However, at 125 K, the majority electron concentration is the largest carrier density and $\tau_{SRH} = \tau_{p_0}$, for the case of n-type material with low injection. With these considerations, Eq. 5.4 becomes

$$\tau_{MC}^{-1} = \tau_{p_0 1}^{-1} + \tau_{p_0 2}^{-1} + \frac{B_r}{\phi} n_0 + C_n n_0^2 \tag{5.5}$$

where $\tau_{p_0 1}$ corresponds to the SRH lifetime of the native defect and $\tau_{p_0 2}$ corresponds to the defect created by the intentional dopant. While $\tau_{p_0 1}$ is considered independent from the doping level (since the associated trap concentration is determined by factors other than the doping concentration), it is assumed $\tau_{p_0 2}$ scales with n_0. In general,

$$\tau_{p_0} = (\sigma_p \nu_p N_t)^{-1} \tag{5.6}$$

where σ_p is the hole defect capture cross-section, ν_p is the hole thermal velocity, and

N_t is the trap density. The simplest case for τ_{p_02} is to assume uncompensated doping, and that every dopant atom creates an SRH recombination center, so that $N_t = n_0$. Prior to fitting the data in Fig. 5.2, the intrinsic radiative recombination coefficient is fixed based on results from Ref. [2], which calculates $B_r = 1.01 \times 10^{-10}$ cm^3/s and provides experimental evidence that $\phi = 15$ for similar MWIR InAs/InAs$_{1-x}$Sb$_x$ T2SLs. The thermal hole velocity used is 2×10^7 cm/s, determined using a **k·p**-calculated density-of-states heavy hole mass of $0.157m_0$. With these parameters, the measured minority carrier lifetime data are best represented using $\tau_{p_01} = 10$ μs, $\sigma_{p2} = 1.7 \times 10^{-18}$ cm^2, and $C_n = 1.6 \times 10^{-26}$ cm^6/s. The Auger coefficient is consistent with those experimentally measured in MWIR InAs/InAs$_{1-x}$Sb$_x$ T2SLs of similar bandgap and composition.[20] The exact T2SL structure has been shown to slightly effect Auger resonances,[20] so because this sample survey includes a range of alloy compositions, the Auger coefficient reported here can be considered an average.

Eq. 5.5 shows the dependence that minority carrier lifetime has with doping level, and highlights the importance of identifying not only the limiting carrier recombination mechanism, but also the optimal doping level. For instance, combining Eq. 5.1 with an Auger-limited minority carrier lifetime (i.e. $\tau_{MC} \approx 1/(C_n n_0^2)$) causes the diffusion current to increase with greater doping level, as shown in Fig. 5.3 by the decrease in $n_0\tau_{MC}$ associated with the Auger component. It is readily observed that the ideal doping density for minimizing dark diffusion current is $n_0 \simeq 2.5 \times 10^{15} cm^{-3}$, the doping level at which $n_0\tau_{MC}$ reaches a maximum. The individual recombination components identified in Fig. 5.2 have also been translated into Fig. 5.3 to highlight where each mechanism limits the $n_0\tau_{MC}$ product. This maximum in the experimen-

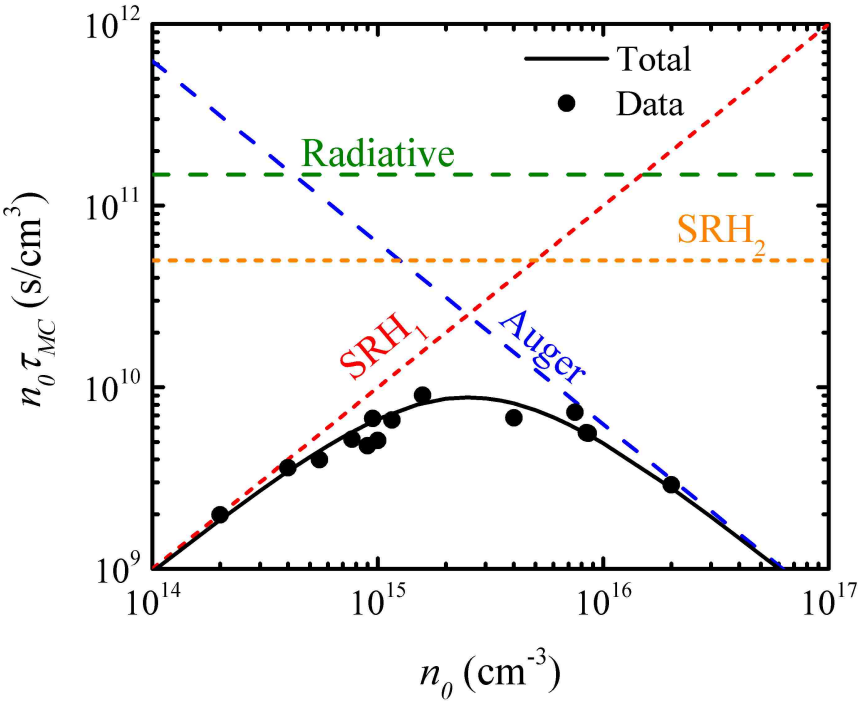

Figure 5.3: Product of $n_0\tau_{MC}$ as a function of doping density at a temperature of 125 K. The solid black curve is a best fit to the data using the same fit parameters as in Fig. 5.2. The colored curves correspond to the individual carrier recombination mechanism that make up the total $n_0\tau_{MC}$ product. SRH_1 and SRH_2 correspond to the SRH recombination associated with native defects and defects created by intentional dopants, respectively.

tal $n_0\tau_{MC}$ product coincides with the transition point from being limited by native defects (SRH_1) to Auger recombination. Clearly, the native defects are a hindrance to attaining larger $n_0\tau_{MC}$ products at doping levels lower than $n_0 = 2.5 \times 10^{15}$ cm^{-3}. Continued efforts to mitigate native defects in InAs/InAs$_{1-x}$Sb$_x$ T2SLs are therefore warranted. A secondary limitation arises from the intentional dopants and τ_{SRH_2}, which would begin to limit the $n_0\tau_{MC}$ product if the native defects are mitigated. However, little is known about how dopants are assimilated into the T2SL structures. Continued research is necessary to verify that intentional dopants do, indeed, create

SRH recombination centers in the T2SL materials.

For doping levels greater than $n_0 = 2.5 \times 10^{15}$ cm^{-3}, Auger recombination is the limiting mechanism. Previous studies on the effects of layer thickness and alloy composition in MWIR InAs/InAs$_{1-x}$Sb$_x$ T2SLs indicate that only minor suppression of Auger recombination is possible while still attaining an approximate 5.2 μm bandgap and keeping strain balanced,[21] suggesting that further improvement of $n_0\tau_{MC}$ at higher doping levels may prove difficult for this wavelength range. Improvements in the Auger recombination will likely require additional materials to be used in the formation of the SL structure, such as the recent demonstration of InGaAs/InAsSb superlattices,[22] in order to provide greater versatility in manipulation of the electronic band structure to suppress Auger resonances.

Fig. 5.4(a) shows dark current as a function of bias voltage at various temperatures for two MWIR InAs/InAs$_{1-x}$Sb$_x$ photodetectors. One has a *nid* absorber (2×10^{14} cm^{-3}) and the second is intentionally doped at a level of 7.5×10^{15} cm^{-3}. Both have 4 μm thick T2SL absorbing layers of similar bandgap energies, 231 meV for the *nid* sample and 219 meV for the doped sample at 100 K. The minority carrier lifetime was measured to be 9.93 μs for the *nid* sample and 0.97 μs for the higher doped sample at 125 K. Minimal variation in the minority carrier lifetime and doping level within the temperature range of 100 - 200 K has been shown previously.[2], [19] The doping levels have been confirmed using the TMR analysis described here. All other device structure layers are nominally the same. Arrhenius plots are shown in Fig. 5.4(b) for a voltage of -0.2 V. Experimental data is compared to generalized temperature trends of diffusion current ($J_{diff} \propto T^3 e^{-E_g/k_B T}$).[15] The *nid* sample shows slight differences with this temperature trend, which are most likely due to

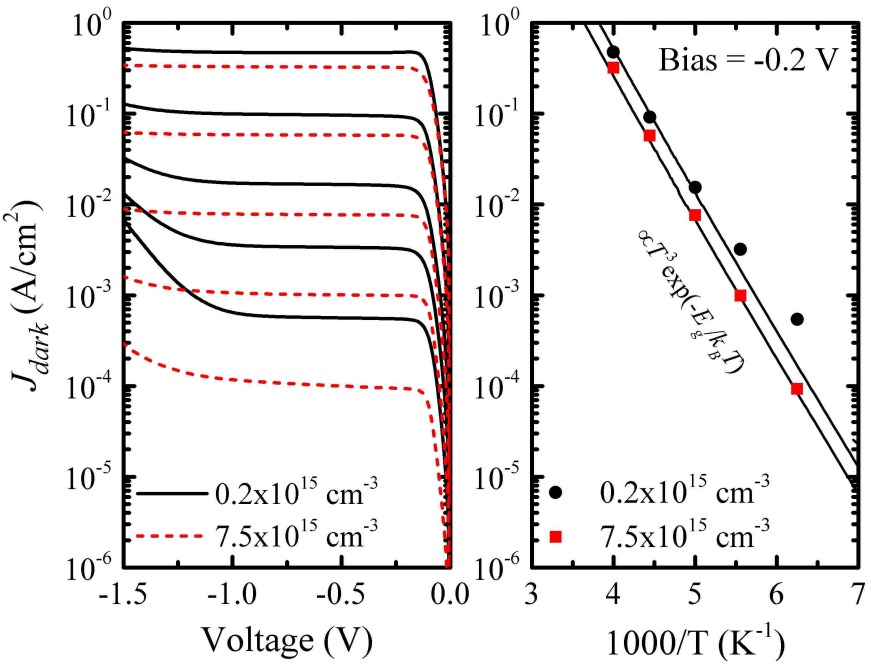

Figure 5.4: (a) Dark current as a function of bias voltage for two MWIR InAs/In As_{1-x} Sb_x photodetectors of different doping levels, for temperatures of 160 to 200 K in steps of 20 K, 225 K, and 250 K. The lowest curves for each sample correspond to 160 K and the highest curves to 250 K. Negative voltages correspond to reverse bias. (b) Arrhenius plots for a bias of -0.2 V. The solid curves correspond to temperature trends of diffusion current.

contributions of generation-recombination (G-R) current. An in-depth analysis of G-R current in InAs/$InAs_{1-x}Sb_x$ T2SLs can be found in Ref. [23].

The diffusion current component of the dark current, which is dominant at temperatures above 160 K for each sample, is shown to be suppressed in the higher doped T2SL. The $n_0\tau_{MC}$ product of the two presented samples are 7.27×10^9 cm^{-3}s for the higher doped sample and 2×10^9 cm^{-3}s for the *nid* sample. Taking into account the difference in n_i of the two samples due to differences in bandgap energy at 200 K, the calculated diffusion current ratio is 1.8 while the measured ratio is 2, demonstrating

a close agreement.

5.4 Conclusion

In summary, time-resolved microwave reflectance was used to extract both minority carrier lifetimes and doping levels for MWIR InAs/$InAs_{1-x}Sb_x$ T2SLs over a range of doping levels. The minority carrier lifetime is found to be dominated by Auger recombination at high doping concentrations, $n_0 > 2.5 \times 10^{15}$ cm^{-3}, and Shockley-Read-Hall recombination through native defects at low doping concentrations, $n_0 < 2.5 \times 10^{15}$ cm^{-3}. We do not find that radiative recombination impacts the carrier lifetime significantly. For optimal reduction in dark diffusion current the $n_0\tau_{MC}$ product must be at a maximum, which was found at a doping level of $n_0 \simeq 2.5 \times 10^{15} cm^{-3}$. This maximum lies at the transition between SRH limited behavior from native defects at lower doping levels and Auger recombination at higher doping levels. Depending on the targeted doping level, further reduction in dark diffusion current (greater $n_0\tau_{MC}$ products) will require mitigation of native SRH defects or suppressing Auger recombination through engineering of the electronic band structure.

Sandia National Laboratories is a multi-program laboratory managed and operated by Sandia Corporation, a wholly owned subsidiary of Lockheed Martin Corporation, for the U.S. Department of Energy's National Nuclear Security Administration under contract DE-AC04-94AL85000. This work was supported by the U.S. Department of Energy, Office of Science, Basic Energy Sciences, Materials Sciences and Engineering Division.

5.5 References

[1] M. A. Kinch, "Fundamental physics of infrared detector materials," *J. Electron. Mat.*, vol. 29, pp. 809–817, 2000.

[2] B. V. Olson, E. A. Kadlec, J. K. Kim, J. F. Klem, S. D. Hawkins, E. A. Shaner, and M. E. Flatté, "Intensity- and temperature-dependent carrier recombination in InAs/Inas1 – $x$sb$x$ type-ii superlattices," *Phys. Rev. Applied*, vol. 3, p. 044 010, 4 2015. DOI: 10.1103/PhysRevApplied.3.044010. [Online]. Available: http://link.aps.org/doi/10.1103/PhysRevApplied.3.044010.

[3] D. R. Rhiger, "Performance comparison of long-wavelength infrared type-ii superlattice devices with HgCdTe," *J. Electron. Mat.*, vol. 40, pp. 1815–1822, 2011.

[4] W. E. Tennant, D. Lee, M. Zandian, E. Piquette, and M. Carmody, "MBE HgCdTe technology: A very general solution to IR detection, described by Rule 07, a very convenient heuristic," *J. Electron. Mat.*, vol. 37, pp. 1406–1410, 2008.

[5] C. H. Grein, P. M. Young, and H. Ehrenreich, "Minority carrier lifetimes in ideal InGaSb/InAs superlattices," *Appl. Phys. Lett.*, vol. 61, pp. 2905–2907, 1992.

[6] C. H. Grein, H. Cruz, M. E. Flatté, and H. Ehrenreich, "Theoretical performance of very long wavelength InAs/InGaSb superlattice based infrared detectors," *Appl. Phys. Lett.*, vol. 65, pp. 2530–5232, 1994.

[7] E. R. Youngdale, J. R. Meyer, C. A. Hoffman, F. J. Bartoli, C. H. Grein, P. M. Young, H. Ehrenreich, R. H. Miles, and D. H. Chow, "Auger lifetime

enhancement in InAs-$Ga_{1-x}In_xSb$ superlattices," *Appl. Phys. Lett.*, vol. 64, pp. 3160–3162, 1994.

[8] S. P. Svensson, D. Donetsky, D. Wang, H. Hier, F. J. Crowne, and G. Belenky, "Growth of type II strained layer superlattice, bulk InAs and GaSb materials for minority lifetime characterization," *J. Crystal Growth*, vol. 334, pp. 103–107, 2011.

[9] D. Donetsky, S. P. Svensson, L. E. Vorobjev, and G. Belenky, "Carrier lifetime measurements in short-period InAs/GaSb strained-layer superlattice structures," *Appl. Phys. Lett.*, vol. 95, p. 212 104, 2009.

[10] B. C. Connelly, G. D. Metcalfe, H. Shen, and M. Wraback, "Direct minority carrier lifetime measurements and recombination mechanisms in long-wave infrared type II superlattices using time-resolved photoluminescence," *Appl. Phys. Lett.*, vol. 97, p. 251 117, 2010.

[11] E. H. Steenbergen, B. C. Connelly, G. D. Metcalfe, H. Shen, M. Wraback, D. Lubyshev, Y. Qiu, J. M. Fastenau, A. W. K. Liu, S. Elhamri, O. O. Cellek, and Y.-H. Zhang, "Significantly improved minority carrier lifetime observed in a long-wavelength infrared III-V type-II superlattice comprised of InAs/InAsSb," *Appl. Phys. Lett.*, vol. 99, p. 251 110, 2011.

[12] B. V. Olson, E. A. Shaner, J. K. Kim, J. F. Klem, S. D. Hawkins, L. M. Murray, J. P. Prineas, M. E. Flatté, and T. F. Boggess, "Time-resolved optical measurements of minority carrier recombination in a mid-wave infrared InAsSb alloy and InAs/InAsSb superlattice," *Appl. Phys. Lett.*, vol. 101, p. 092 109, 2012.

[13] L. Höglund, D. Z. Ting, A. Khoshakhlagh, A. Soibel, C. J. Hill, A. Fisher, S. Keo, and S. D. Gunapala, "Influence of radiative and non-radiative recombination on the minority carrier lifetime in midwave infrared inas/inassb superlattices," *Appl. Phys. Lett.*, vol. 103, no. 22, 221908, 2013. DOI: http://dx.doi.org/10.1063/1.4835055. [Online]. Available: http://scitation.aip.org/content/aip/journal/apl/103/22/10.1063/1.4835055.

[14] L. Höglund, D. Z. Ting, A. Soibel, A. Fisher, A. Khoshakhlagh, C. J. Hill, S. Keo, and S. D. Gunapala, "Minority carrier lifetime in mid-wavelength infrared InAs/InAsSb superlattices: Photon recycling and the role of radiative and shockley-read-hall recombination mechanisms," *Appl. Phys. Lett.*, vol. 105, no. 19, 193510, 2014. DOI: http://dx.doi.org/10.1063/1.4902022. [Online]. Available: http://scitation.aip.org/content/aip/journal/apl/105/19/10.1063/1.4902022.

[15] B. V. Olson, C. H. Grein, J. K. Kim, E. A. Kadlec, J. F. Klem, S. D. Hawkins, and E. A. Shaner, "Auger recombination in long-wave infrared inas/inassb type-ii superlattices," *Appl. Phys. Lett.*, vol. 107, no. 26, 261104, 2015. DOI: http://dx.doi.org/10.1063/1.4939147. [Online]. Available: http://scitation.aip.org/content/aip/journal/apl/107/26/10.1063/1.4939147.

[16] B. V. Olson, J. K. Kim, E. A. Kadlec, J. F. Klem, S. D. Hawkins, D. Leonhardt, W. T. Coon, T. R. Fortune, M. A. Cavaliere, A. Tauke-Pedretti, and E. A. Shaner, "Minority carrier lifetime and dark current measurements in mid-wavelength infrared InAs0.91Sb0.09 alloy nbn photodetectors," *Appl. Phys. Lett.*, vol. 107, no. 18, 183504, 2015. DOI: http://dx.doi.org/10.1063/

1.4935159. [Online]. Available: http://scitation.aip.org/content/aip/journal/apl/107/18/10.1063/1.4935159.

[17] R. N. Hall, "Recombination processes in semicondcutors," *Proc. of IEE*, vol. 106, pp. 923–931, 1959.

[18] S. Cervera, J. B. Rodriquez, J. P. Perez, H. Aït-Kaci, R. Chaghi, L. Konczewicz, S. Contreras, and P. Christol, "Unambiguous determination of carrier concentration and mobility for InAs/GaSb superlattice photodiode optimization," *J. Appl. Phys.*, vol. 106, p. 033 709, 2009.

[19] B. V. Olson, E. A. Shaner, J. K. Kim, J. F. Klem, S. D. Hawkins, M. E. Flatté, and T. F. Boggess, "Identification of dominant recombination mechanisms in narrow-bandgap InAs/InAsSb type-II superlattices and InAsSb alloys," *Appl. Phys. Lett.*, vol. 103, p. 052 106, 2013.

[20] Y. Aytac, B. V. Olson, J. K. Kim, E. A. Shaner, S. D. Hawkins, J. F. Klem, M. E. Flatt, and T. F. Boggess, "Temperature-dependent optical measurements of the dominant recombination mechanisms in inas/inassb type-2 superlattices," *Journal of Applied Physics*, vol. 118, no. 12, 125701, 2015. DOI: http://dx.doi.org/10.1063/1.4931419. [Online]. Available: http://scitation.aip.org/content/aip/journal/jap/118/12/10.1063/1.4931419.

[21] ——, "Effects of layer thickness and alloy composition on carrier lifetimes in mid-wave infrared inas/inassb superlattices," *Applied Physics Letters*, vol. 105, no. 2, 022107, 2014. DOI: http://dx.doi.org/10.1063/1.4890578. [Online]. Available: http://scitation.aip.org/content/aip/journal/apl/105/2/10.1063/1.4890578.

[22] G. Ariyawansa, C. J. Reyner, E. H. Steenbergen, J. M. Duran, J. D. Reding, J. E. Scheihing, H. R. Bourassa, B. L. Liang, and D. L. Huffaker, "Ingaas/inassb strained layer superlattices for mid-wave infrared detectors," *Appl. Phys. Lett.*, vol. 108, no. 2, 022106, 2016. DOI: http://dx.doi.org/10.1063/1.4939904. [Online]. Available: http://scitation.aip.org/content/aip/journal/apl/108/2/10.1063/1.4939904.

[23] D. R. Rhiger, E. P. Smith, B. P. Kolasa, J. K. Kim, J. F. Klem, and S. D. Hawkins, "Analysis of iii–v superlattice nbn device characteristics," *Journal of Electronic Materials*, vol. 45, no. 9, pp. 4646–4653, 2016, ISSN: 1543-186X. DOI: 10.1007/s11664-016-4545-y. [Online]. Available: http://dx.doi.org/10.1007/s11664-016-4545-y.

Chapter 6

Conclusion and Future Work

6.1 Conclusion

The importance of non-invasive (i.e. non-contact) carrier lifetime measurements is demonstrated in this dissertation through the investigation of recombination mechanisms and doping density of an InAs/InAsSb MWIR T2SL. Three main topics were presented: a comparison of common lifetime measurement techniques based on both photoluminescence and microwave reflectance, an extension of the frequency modulated technique to large modulation, and using time-resolved microwave reflectance measurements to probe doping density and lifetime to predict device performance.

6.1.1 Common Lifetime measurement comparison

Carrier lifetime analysis can provide vital information on the quality of semiconductor material and how well that material will perform in use for specific appli-

cations. For example, the minority carrier lifetime can be directly related to dark-diffusion currents in a photodetector [1], [2]. There are many different carrier lifetime measurement techniques. For direct-band semiconductors, photoluminescence-based measurements tend to be the most popular as these are most conducive to optical labs [3]–[6]. Another method of lifetime measurement is to probe the decay with microwave radiation, which has no dependence on the bandgap energy of the material under test. This method has shown great promise for use in both MWIR and LWIR InAs/InAsSb T2SL lifetime measurements [2], [7]–[9].

A brief comparison of photoluminescence and microwave reflectance-based lifetime measurement techniques was show in Chapter 3 of this dissertation. This comparison revealed that although photoluminescence-based lifetime measurement systems are more common in literature, microwave reflectance-based systems do outperform them in both sensitivity and flexibility (i.e. is not bandgap dependent). The time-resolved microwave reflectance setup shown in this dissertation obtained sensitivities of $\approx 10^{13} - 10^{14}$ cm^{-3}, roughly an order of magnitude better than the photoluminescence-based systems. It should be noted, however, that photoluminescence is still a viable means of measuring carrier lifetime.

6.1.2 Frequency modulated large-modulation technique

A common method of lifetime measurement, known as frequency-modulated continuous wave or optical modulation response, uses a DC laser with a small AC modulation to generate carriers. The frequency of the modulation is swept resulting in an AC roll-off of modulated carriers. This roll-off, which is proportional to the carrier life-

time, can be measured by photoluminescence or probed by microwave reflectance, as shown in Chapter 3. The steady-state carrier density is found from the product of the DC generation term and carrier lifetime found from the AC roll-off. A major limitation of this method is investigating large carrier densities, which are needed to properly measure Auger recombination. At first glance, one would think the easiest way to reach large carrier densities is to focus the laser spot size, however the spot size is eventually limited by carrier diffusion, thus, limiting carrier density. A way to investigate Auger recombination is to use large modulation, instead of the more-common small modulation.

In Chapter 4, the frequency modulated technique was investigated by numerical simulation showing that higher harmonic terms resultant of radiative and Auger recombination are generated in the carrier density. It was shown that these terms are more prevalent with large modulation than small modulation. Recombination mechanism measurements using a large modulation generation were made on an InAs/InAsSb T2SL. The results matched simulation and agreed with the more-readily used TMR method. As a bonus, these measurements also showed that the small modulation technique can serve as a excellent measurement of minority carrier lifetime.

6.1.3 Predicting device performance

Time-resolved microwave reflectance was used to extract both minority carrier lifetimes and doping levels for MWIR InAs/$InAs_{1-x}Sb_x$ T2SLs over a range of doping levels. The minority carrier lifetime is found to be dominated by Auger recombina-

tion at high doping concentrations, $n_0 > 2.5 \times 10^{15}$ cm^{-3}, and Shockley-Read-Hall recombination through native defects at low doping concentrations, $n_0 < 2.5 \times 10^{15}$ cm^{-3}. We do not find that radiative recombination impacts the carrier lifetime significantly. For optimal reduction in dark diffusion current the $n_0\tau_{MC}$ product must be at a maximum, which was found at a doping level of $n_0 \simeq 2.5 \times 10^{15} cm^{-3}$. This maximum lies at the transition between SRH limited behavior from native defects at lower doping levels and Auger recombination at higher doping levels. Depending on the targeted doping level, further reduction in dark diffusion current (greater $n_0\tau_{MC}$ products) will require mitigation of native SRH defects or suppressing Auger recombination through engineering of the electronic band structure.

6.2 Future Work

6.2.1 Vertical transport

The InAs/InAsSb T2SL has received increased attention due to the long minority carrier lifetimes showing potential for use as a LWIR detector material. Localization in the vertical transport measurements has recently been revealed and is hypothesized to be due to nanoscale fluctuations in the InAsSb alloy layers, as well as the individual atoms of the Sb that have diffused into the InAs layer during growth. These features are highlighted in the atomic scale cross-sectional STM image in Fig. 6.1(e). Although this technologically important material system has seen recent elevated investigation, to date there has only been a single vertical transport measurement performed [10]. Unlike in-plane transport, which can be similar to that of bulk ma-

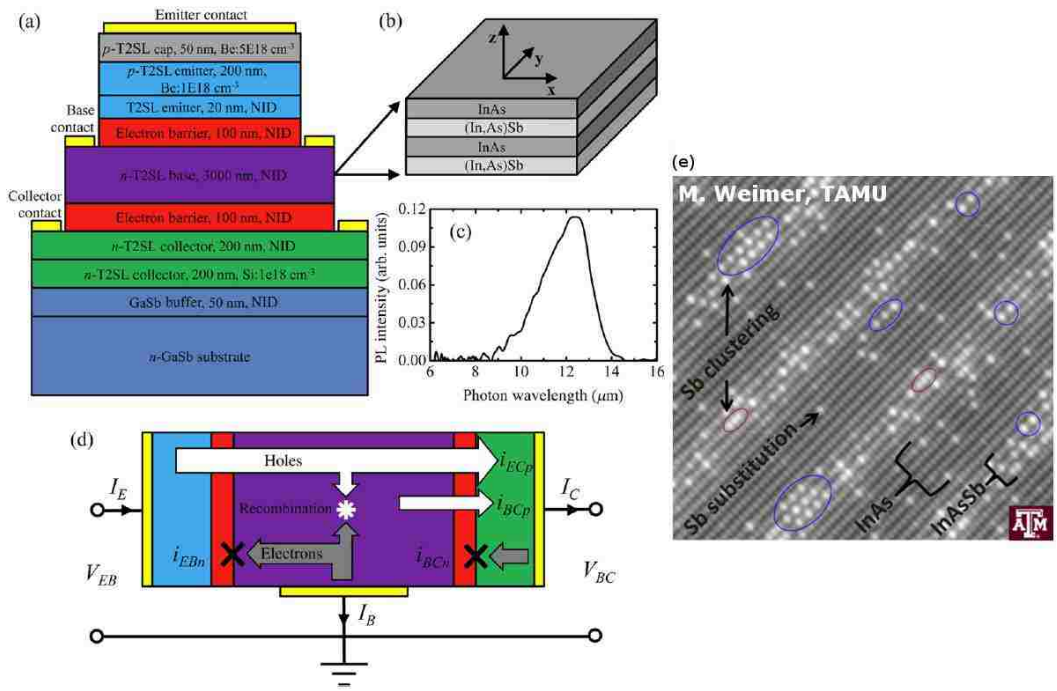

Figure 6.1: (a) Schematic of the T2SL HBT epitaxial growth structure. (b) Enlarged view of the T2SL layers with the axes defining the transport directions: x, y are the in-plane directions and z is the vertical direction. (c) 18 K photoluminescence from the HBT structures demonstrating the long-wave infrared bandgap energy of the T2SL layers. (d) Electrical schematic of the T2SL HBT device in the common-base configuration with the various current identified [10]. (e) Anion image from large-area STM survey of superlattice periods [11]

terial, vertical transport is significantly different from bulk charge transport due to the presence of the naometer scale and periodic potential wells along the growth axis [12], [13]. Conventional transport measurements such as Hall effect can suffice for in-plane diagnostics, however vertical transport is much more challenging. A unique approach to the measurement of vertical transport would be to use InAs/InAsSb T2SL based heterojunction bipolar transistor (HBT) devices [10]. HBTs are a minority carrier transport device and provide an ideal platform with which to study

fundamental transport properties in these narrow-bandgap semiconductors. A diagram of the proposed device can be seen in Fig. 6.1(a) with the resulting carrier dynamics shown in Fig. 6.1(d). A recent study by Wood *et. al* [11] has shown antimony cross-incorporation in the InAs layer of the superlattice (Fig. 6.1(e)).

6.2.2 Radiation effects

Recent studies of the effects of 63 MeV proton radiation on InAs/InAsSb T2SLs have shown degradation of quantum efficiency (QE) and rise in dark current with increased dose of proton radiation [14]. It was suggested from these results that the effects were due to decreases of the minority carrier lifetime as a result of the proton radiation. A more recent study has investigated the minority carrier lifetime as a function of 68 MeV proton radiation dose [15]. The results of this study have shown that the minority carrier lifetime does indeed decrease with increase proton radiation due to the introduction of SRH trap centers induced from proton radiation damage. The results of these two studies suggest proton radiation negatively affects the material quality, as would be predicted. As a continuation of these studies, an in-situ measurement of carrier lifetime as a function of radiation dose and time post radiation should be made. Results from these measurements could provide information of predicted performance for in-the-field devices.

6.3 References

[1] D. R. Rhiger, E. P. Smith, B. P. Kolasa, J. K. Kim, J. F. Klem, and S. D. Hawkins, "Analysis of iii–v superlattice nbn device characteristics," *Journal of*

Electronic Materials, vol. 45, no. 9, pp. 4646–4653, 2016, ISSN: 1543-186X. DOI: 10.1007/s11664-016-4545-y. [Online]. Available: http://dx.doi.org/10.1007/s11664-016-4545-y.

[2] E. A. Kadlec, B. V. Olson, M. D. Goldflam, J. K. Kim, J. F. Klem, S. D. Hawkins, W. T. Coon, M. A. Cavaliere, A. Tauke-Pedretti, T. R. Fortune, C. T. Harris, and E. A. Shaner, "Effects of electron doping level on minority carrier lifetimes in n-type mid-wave infrared inas/inas1xsbx type-ii superlattices," *Applied Physics Letters*, vol. 109, no. 26, p. 261 105, 2016. DOI: 10.1063/1.4973352. eprint: http://dx.doi.org/10.1063/1.4973352. [Online]. Available: http://dx.doi.org/10.1063/1.4973352.

[3] B. C. Connelly, G. D. Metcalfe, H. Shen, and M. Wraback, "Time-resolved photoluminescence study of carrier recombination and transport in type-II superlattice infrared detector materials," *Proc. of SPIE*, vol. 8704, pp. 87040V–1, 2013.

[4] ——, "Direct minority carrier lifetime measurements and recombination mechanisms in long-wave infrared type II superlattices using time-resolved photoluminescence," *Appl. Phys. Lett.*, vol. 97, p. 251 117, 2010.

[5] E. H. Steenbergen, B. C. Connelly, G. D. Metcalfe, H. Shen, M. Wraback, D. Lubyshev, Y. Qiu, J. M. Fastenau, A. W. K. Liu, S. Elhamri, O. O. Cellek, and Y.-H. Zhang, "Significantly improved minority carrier lifetime observed in a long-wavelength infrared III-V type-II superlattice comprised of InAs/InAsSb," *Appl. Phys. Lett.*, vol. 99, p. 251 110, 2011.

[6] D. Donetsky, S. P. Svensson, L. E. Vorobjev, and G. Belenky, "Carrier lifetime measurements in short-period InAs/GaSb strained-layer superlattice structures," *Appl. Phys. Lett.*, vol. 95, p. 212 104, 2009.

[7] B. V. Olson, E. A. Kadlec, J. K. Kim, J. F. Klem, S. D. Hawkins, E. A. Shaner, and M. E. Flatté, "Intensity- and temperature-dependent carrier recombination in InAs/Inas1 $-$ $x$sb$x$ type-ii superlattices," *Phys. Rev. Applied*, vol. 3, p. 044 010, 4 2015. DOI: 10.1103/PhysRevApplied.3.044010. [Online]. Available: http://link.aps.org/doi/10.1103/PhysRevApplied.3.044010.

[8] B. V. Olson, C. H. Grein, J. K. Kim, E. A. Kadlec, J. F. Klem, S. D. Hawkins, and E. A. Shaner, "Auger recombination in long-wave infrared inas/inassb type-ii superlattices," *Appl. Phys. Lett.*, vol. 107, no. 26, 261104, 2015. DOI: http://dx.doi.org/10.1063/1.4939147. [Online]. Available: http://scitation.aip.org/content/aip/journal/apl/107/26/10.1063/1.4939147.

[9] B. V. Olson, E. A. Kadlec, J. K. Kim, J. F. Klem, S. D. Hawkins, A. Tauke-Pedretti, W. T. Coon, T. R. Fortune, and E. A. Shaner, "Contactless measurement of equilibrium electron concentrations in n-type inas/inas1xsbx type-ii superlattices," *Applied Physics Letters*, vol. 109, no. 2, 022105, 2016. DOI: http://dx.doi.org/10.1063/1.4956351. [Online]. Available: http://scitation.aip.org/content/aip/journal/apl/109/2/10.1063/1.4956351.

[10] B. V. Olson, J. F. Klem, E. A. Kadlec, J. K. Kim, M. D. Goldflam, S. D. Hawkins, A. Tauke-Pedretti, W. T. Coon, T. R. Fortune, E. A. Shaner, and M. E. Flatté, "Vertical hole transport and carrier localization in InAs/inas1 $-$ $x$sb$x$ type-ii superlattice heterojunction bipo-

lar transistors," *Phys. Rev. Applied*, vol. 7, p. 024 016, 2 2017. DOI: 10.1103/PhysRevApplied.7.024016. [Online]. Available: http://link.aps.org/doi/10.1103/PhysRevApplied.7.024016.

[11] M. Wood, K. Kanedy, F. Lopez, M. Weimer, J. Klem, S. Hawkins, E. Shaner, and J. Kim, "Monolayer-by-monolayer compositional analysis of inas/inassb superlattices with cross-sectional {stm}," *Journal of Crystal Growth*, vol. 425, pp. 110 –114, 2015, The 18th International Conference on Molecular Beam Epitaxy (MBE 2014), ISSN: 0022-0248. DOI: http://dx.doi.org/10.1016/j.jcrysgro.2015.02.063. [Online]. Available: http://www.sciencedirect.com/science/article/pii/S0022024815001530.

[12] B. Deveaud, J. Shah, T. C. Damen, B. Lambert, and A. Regreny, "Bloch transport of electrons and holes in superlattice minibands: Direct measurement by subpicosecond luminescence spectroscopy," *Phys. Rev. Lett.*, vol. 58, pp. 2582–2585, 24 1987. DOI: 10.1103/PhysRevLett.58.2582. [Online]. Available: https://link.aps.org/doi/10.1103/PhysRevLett.58.2582.

[13] A. Chomette, B. Deveaud, A. Regreny, and G. Bastard, "Observation of carrier localization in intentionally disordered gaas/gaalas superlattices," *Phys. Rev. Lett.*, vol. 57, pp. 1464–1467, 12 1986. DOI: 10.1103/PhysRevLett.57.1464. [Online]. Available: https://link.aps.org/doi/10.1103/PhysRevLett.57.1464.

[14] C. P. Morath, V. M. Cowan, L. A. Treider, G. D. Jenkins, and J. E. Hubbs, "Proton irradiation effects on the performance of iii-v-based, unipolar barrier infrared detectors," *IEEE Transactions on Nuclear Science*, vol. 62, no. 2, pp. 512–519, 2015.

[15] L. Höglund, D. Z. Ting, A. Khoshakhlagh, A. Soibel, A. Fisher, C. J. Hill, S. Keo, S. Rafol, and S. D. Gunapala, "Influence of proton radiation on the minority carrier lifetime in midwave infrared inas/inassb superlattices," *Applied Physics Letters*, vol. 108, no. 26, 263504, 2016. DOI: http://dx.doi.org/10.1063/1.4954901. [Online]. Available: http://scitation.aip.org/content/aip/journal/apl/108/26/10.1063/1.4954901.